A numerical spectral approach for solving elasto-static field dislocation and g-disclination mechanics

Stéphane Berbenni *, Vincent Taupin, Komlan Sénam Djaka, Claude Fressengeas

Laboratoire d'Etude des Microstructures et de Mécanique des Matériaux, LEM3, UMR CNRS 7239, University of Lorraine, Ile du Saulcy, 57045 Metz, France

ABSTRACT

A spectral approach is developed to solve the elasto-static equations of field dislocation and g-disclination mechanics in periodic media. Given the spatial distribution of Nye's dislocation density and/or g-disclination density tensors in heterogeneous or homogenous linear elastic media, the incompatible and compatible elastic distortions are respectively obtained from the solutions of Poisson and Navier-type equations in the Fourier space. Intrinsic discrete Fourier transforms solved by the Fast Fourier Transform (FFT) method, which are consistent with the pixel grid for the calculation of first and second order spatial derivatives, are preferred and compared to the classical discrete approximation of continuous Fourier transforms when deriving elastic fields of defects. Numerical examples are provided for homogeneous linear elastic isotropic solids. For various defects, a regularized defect density in the core is considered and smooth elastic fields without Gibbs oscillations are obtained, when using intrinsic discrete Fourier transforms. The results include the elastic fields of single screw and edge dislocations, standard wedge disclinations and associated dipoles, as well as "twinning g-disclinations". In order to validate the present spectral approach, comparisons are made with analytical solutions using the Riemann–Graves integral operator and with numerical simulations using the finite element approximation.

© 2014 Elsevier Ltd. All rights reserved.

1. Introduction

In crystalline media, the internal stresses result from the residual elastic displacements of atoms from their low-energy equilibrium positions when the applied loading is removed. Such deformed configurations stem from an incompatible process where crystal defects – dislocations, disclinations or "generalized disclinations" (abbreviated "g-disclinations") – induce the discontinuity of elastic displacement or distortion across surfaces in the body. Dislocations and disclinations were simultaneously introduced by Volterra in his seminal 1907 paper (Volterra, 1907). In the sole presence of dislocations, the elastic displacement vector is a multi-valued function along some (non-unique) surface, whereas the elastic rotation remains continuous. The discontinuity of the elastic displacement derives from the incompatibility of the elastic strain, whereas the elastic curvature tensor remains compatible. This limited state of incompatibility was described smoothly in the elastic theory of continuously distributed dislocations (ECDD) initiated by Kröner (1958, 1981) and others (Bilby et al., 1955; deWit, 1960; Mura, 1963; Willis, 1967; Kosevich,

1979) by using Nye's dislocation density tensor. ECDD was recently revisited by Acharya (2001); Roy and Acharya (2005) and Acharya and Roy (2006). One of the key features of the revisited ECDD theory resides in the Stokes–Helmholtz decomposition of the elastic distortion and the complementary conditions yielding a unique solution for the incompatible part associated with a prescribed dislocation density field, while the compatible part is unambiguously determined from the satisfaction of the balance of momentum and boundary conditions.

When disclinations are present in the body in addition to dislocations, the elastic displacement and rotation vectors are both multi-valued functions. Such a situation typically occurs in solids exhibiting kink bands, grain and subgrain boundaries and triple junctions. In this case, the elastic curvature tensor has an incompatible part complementing the compatible gradient component (deWit, 1970; Fressengeas et al., 2011). Beyond Volterra's construct, the entire elastic distortion tensor (including the elastic strain tensor in addition to the elastic rotation tensor) may be multivalued along some surface. Such situations are commonplace. They include terminating twinning and phase transformation interfaces (phase boundaries), terminating shear bands, sharp corners of inclusions in a matrix of dissimilar material, etc..., in addition to grain boundaries and triple junctions. As recently discussed by Acharya and

Fressengeas (2012), the discontinuity of the elastic distortion is reflected by the incompatibility of the elastic 2-distortion (*i.e.* the second gradient of displacement in gradient elasticity), in the presence of a non-vanishing g-disclination density tensor field.

When the crystal defects are viewed at sufficiently small scale, there are actually no discontinuities but only appropriately localized smooth fields, possibly featuring strong gradients. Such a smooth localized representation of the physical reality of the defects is essential from the point of view of mathematical analysis and numerical computation, and for the rendition of core properties. If a larger scale of resolution is adopted in the above crystal defect field theories, for example when a large polycrystalline sample is considered, smooth areal densities of crystal defects can still be defined, but part of the defects statistically offset each other to a null contribution to incompatibility and the overall residual stress level becomes underestimated in the analysis. Therefore, it is essential that a numerical scheme for the determination of the residual stresses is able to probe the whole range of resolution length scales to provide appropriate estimates. The finite element method (FEM) has allowed implementing the elastic theory of continuously distributed dislocations and disclinations at various length scales. For example it was used at mesoscale to determine uniquely both the incompatible and compatible elastic distortion in the field theory of dislocation mechanics (Roy and Acharya, 2005). At nanoscale, the field theory of dislocation and disclination mechanics has allowed retrieving the elastic energy of [001] copper symmetric tilt grain boundaries with a good accuracy at all misorientations (Fressengeas et al., 2014).

An increasingly attractive alternative to the finite element method is a computationally efficient scheme based on the Fast Fourier Transform (FFT) for the solution of periodic boundary value problems in continuum mechanics (Moulinec and Suquet, 1994; Müller, 1996, 1998; Moulinec and Suquet, 1998; Eyre and Milton, 1999; Dreyer et al., 1999; Herrmann et al., 1999; Lebensohn, 2001; Michel et al., 2001; Neumann et al., 2002; Vinogradov and Milton, 2008; Anglin et al., 2014). This numerical approach solves the Lippmann–Schwinger integral equation of the periodic boundary-value problems by means of the Green's function of a chosen reference medium. It has been applied so far to elastic and elasto-plastic composites and polycrystals in the absence of crystal defects, and very recently for the computation of static mechanical fields due to dislocation-type defects (Brenner et al., 2014). The main interest of the FFT approach relies on its computational efficiency (Moulinec and Suquet, 1998; Prakash and Lebensohn, 2012; Lebensohn et al., 2012; Eisenlohr et al., 2013; Spahn et al., 2014). Its main drawbacks are the need for a periodic representative volume element and the possible occurrence of spurious Gibbs oscillations arising from the presence of strong spatial gradients.

The present paper is dedicated to extending this scheme to the elastic properties of defected media with dislocations and g-disclinations. Rather than dealing with polycrystals and large resolution length scales, the paper will be focused on individual defects and the associated regularized core properties. Special attention will be devoted to the control of the Gibbs phenomenon, which appears to be essential at low resolution length scale for dislocations as well as g-disclinations. The static field equations of continuum dislocation and g-disclination mechanics are reviewed in Section 3. The spectral continuous Fourier-based approach is presented in Section 4. Here, general three-dimensional solutions for incompatible and compatible elastic fields of dislocation and g-disclinations are derived for the first time to compute their internal strain/stress field in the Fourier space. In Section 5, the discrete Fourier transform method is introduced in the case of two-dimensional (2D) problems, and the FFT algorithm is used to solve Poisson and Navier-type equations in the case of infinite straight lines, including dislocations and g-disclinations. In Section 6, dislocation or g-disclination densities are distributed on 2D FFT pixelized grids for different descriptions of dislocation/g-disclination cores. The incompatible and compatible elastic fields are obtained in the discrete Fourier space and then used to derive the stresses, elastic rotations and curvatures by using the inverse FFT for an isotropic elastic solid. The present method is validated by comparisons with existing analytical expressions (deWit, 1970; Hirth and Lothe, 1982; Romanov and Vladimirov, 1992; Acharya, 2001) and with FEM results for the same periodic unit cells. In Section 7, a discussion is provided to show that the present FFT method avoids numerical Gibbs oscillations compared to other methods when dislocation densities are assigned to a single pixel. Section 8 concludes and sketches the perspectives.

2. Notations

A bold symbol denotes a tensor or a vector, except a rotated vector denoted $\vec{\mathbf{V}}$ or a rotated tensor denoted $\tilde{\mathbf{V}}$ to avoid ambiguity (see below). The symmetric part of tensor $\mathbf{A}$ is denoted $\mathbf{A}^{sym}$. Its skew-symmetric part is $\mathbf{A}^{skew}$ and its transpose is denoted by $\mathbf{A}^t$. The tensor $\mathbf{A} \cdot \mathbf{B}$, with rectangular Cartesian components $A_{ik}B_{kj}$, results from the dot product of tensors $\mathbf{A}$ and $\mathbf{B}$, and $\mathbf{A} \otimes \mathbf{B}$ is their tensorial product, with components $A_{ij}B_{kl}$. The vector $\mathbf{A} \cdot \mathbf{V}$, with rectangular Cartesian components $A_{ij}V_j$, results from the dot product of tensor $\mathbf{A}$ and vector $\mathbf{V}$. A : represents the trace inner product of the two second order tensors $\mathbf{A} : \mathbf{B} = A_{ij}B_{ij}$, in rectangular Cartesian components, or the product of a higher order tensor with a second order tensor, e.g., $\mathbf{A} : \mathbf{B} = A_{ijkl}B_{kl}$. The cross product of a second-order tensor $\mathbf{A}$ and a vector $\mathbf{V}$, the **div** and **curl** operations for second/third-order tensors are defined row by row, in analogy with the vectorial case. For any base vector $\mathbf{e}_i$ of the reference frame:

$$(\mathbf{A} \times \mathbf{V})^t \cdot \mathbf{e}_i = (\mathbf{A}^t \cdot \mathbf{e}_i) \times \mathbf{V} \tag{1}$$

$$(\mathbf{div}\, \mathbf{A})^t \cdot \mathbf{e}_i = \mathbf{div}\, (\mathbf{A}^t \cdot \mathbf{e}_i) \tag{2}$$

$$(\mathbf{curl}\, \mathbf{A})^t \cdot \mathbf{e}_i = \mathbf{curl}\, (\mathbf{A}^t \cdot \mathbf{e}_i). \tag{3}$$

In rectangular Cartesian components:

$$(\mathbf{A} \times \mathbf{V})_{ij} = e_{jkl}A_{ik}V_l \tag{4}$$

$$(\mathbf{A} \times \mathbf{V})_{ijk} = e_{klm}A_{ijl}V_m \tag{5}$$

$$(\mathbf{div}\, \mathbf{A})_i = A_{ij,j} \tag{6}$$

$$(\mathbf{div}\, \mathbf{A})_{ij} = A_{ijk,k} \tag{7}$$

$$(\mathbf{curl}\, \mathbf{A})_{ij} = e_{jkl}A_{il,k} = -(\mathbf{grad}\, \mathbf{A} : \mathbf{X})_{ij} \tag{8}$$

$$(\mathbf{curl}\, \mathbf{A})_{ijk} = e_{klm}A_{ijm,l}. \tag{9}$$

where e_{jkl} is a component of the third-order alternating Levi–Civita tensor $\mathbf{X}$ and the spatial derivative with respect to a Cartesian coordinate is indicated by a comma followed by the component index. A rotated vector $\vec{\mathbf{A}}$ is associated with the second order tensor $\mathbf{A}$ by using its trace inner product with tensor $\mathbf{X}$:

$$(\vec{\mathbf{A}})_k = -\frac{1}{2}(\mathbf{A} : \mathbf{X})_k = -\frac{1}{2}e_{ijk}A_{ij}. \tag{10}$$

Similarly, a rotated tensor $\tilde{\mathbf{A}}$ is associated with the third order tensor $\mathbf{A}$ by using its trace inner product with tensor $\mathbf{X}$:

$$(\tilde{\mathbf{A}})_{kl} = -\frac{1}{2}(\mathbf{A} : \mathbf{X})_{kl} = -\frac{1}{2}e_{ijk}A_{ijl}. \tag{11}$$

3. Elasto-static equations of field dislocation and g-disclination mechanics

3.1. Elasto-static field equations

The analysis is developed in the small distortion framework. The body V, with boundary ∂V, is assumed to be a continuum, with

smooth displacement and rotation vector fields ($\mathbf{u}, \vec{\omega} = 1/2$ **curl u**). The total 1-distortion (first distortion) tensor field $\mathbf{U} = \mathbf{grad}\,\mathbf{u}$, the curvature tensor field, $\boldsymbol{\kappa} = \mathbf{grad}\,\vec{\omega}$, and the 2-distortion (second distortion) tensor field, $\mathbf{G} = \mathbf{grad}\,\mathbf{U}$, are therefore assumed to be integrable (compatible, or curl free). Under such assumptions, the possibility of developing cracks or voids in the body is discarded. The total 1-distortion writes as the sum of the elastic distortion, $\mathbf{U}_e$, and plastic (inelastic) distortion, $\mathbf{U}_p$:

$$\mathbf{U} = \mathbf{U}_e + \mathbf{U}_p. \tag{12}$$

Similarly, the 2-distortion tensor can be decomposed into elastic and inelastic 2-distortion tensors:

$$\mathbf{G} = \mathbf{G}_e + \mathbf{G}_p. \tag{13}$$

In a compatible body in the absence of polarized crystal defect density, the elastic/plastic distortions and 2-distortions are curl-free gradient tensors. However, they will contain incompatible, non-gradient parts, in the presence of a polarized crystal defect density, while total 1 and 2-distortions remain compatible. Such incompatibility will be discussed below in Section 3.2. In the present paper, the linear elastic constitutive law (Hooke's law) is specified as:

$$\mathbf{T} = \mathbf{C} : \mathbf{U}_e^{sym} = \mathbf{C} : \boldsymbol{\varepsilon}_e, \tag{14}$$

where $\mathbf{C}$ is the fourth order tensor of linear heterogeneous elastic moduli, with the symmetry properties $C_{ijkl} = C_{jikl} = C_{ijlk} = C_{klij}$, and $\boldsymbol{\varepsilon}_e$ is the elastic strain tensor, or the symmetric part of the elastic distortion tensor. Higher order elastic laws should be considered for consistency when discontinuities of the elastic 2-distortion are present, as shown in Acharya and Fressengeas (2012) and Upadhyay et al. (2013), but they will be neglected here for the sake of simplicity. Hence, only the symmetric Cauchy stress $\mathbf{T}$ is considered and satisfies the balance equation:

$$\mathbf{div}\,\mathbf{T} = 0 \quad \text{in } V, \tag{15}$$

appended with boundary conditions. It is assumed, in a standard manner, that a prescribed traction vector field $\mathbf{t}^d$ is applied to a part ∂V_t of the boundary ∂V, and that the other part ∂V_u is subjected to the prescribed displacements $\mathbf{u}^d$.

3.2. Discontinuity and incompatibility in defected crystals

In his 1907 paper, Volterra introduced six types of crystal line defects (Volterra, 1907). Three of them, known as dislocations, are translational defects, and the other three, referred to as disclinations, are rotational defects. Like disclinations, dislocations have a smooth elastic distortion field $\mathbf{U}_e$ in a non-simply-connected domain excluding their core. However, their elastic/plastic displacement fields ($\mathbf{u}_e/\mathbf{u}_p$) feature a discontinuity ($\llbracket\mathbf{u}_e\rrbracket/\llbracket\mathbf{u}_p\rrbracket$) across a (non-unique) smooth surface in this domain. The geometry of any such surface is arbitrary except that, in a discrete modeling framework, it terminates along the dislocation line. A line integral of the elastic distortion field along any curve encircling the dislocation line, *i.e.* a Burgers circuit, is constant and equal to the discontinuity of the elastic displacement. This constant $\mathbf{b} = \llbracket\mathbf{u}_e\rrbracket$ is referred to as the Burgers vector of the dislocation. It represents the strength of the dislocation. In contrast with Volterra's discrete representation of crystal defects, we presently choose a continuous setting, in order to regularize this classical description. We consider smooth elastic distortion fields in simply connected domains, in which they are point-wise irrotational outside the core region, whereas their non-vanishing curl defines a smooth dislocation density tensor field inside the core (of non-zero volume):

$$\boldsymbol{\alpha} = \mathbf{curl}\,\mathbf{U}_e. \tag{16}$$

The Burgers vector is then obtained by integrating the dislocation density tensor field, referred to as Nye's tensor field, over appropriate surface patches S with unit normal $\mathbf{n}$:

$$\mathbf{b} = \int_S \boldsymbol{\alpha} \cdot \mathbf{n}\,dS. \tag{17}$$

Similarly, disclinations result from a discontinuity ($\llbracket\vec{\omega}_e\rrbracket, \llbracket\vec{\omega}_p\rrbracket$) in the elastic/plastic rotation fields ($\vec{\omega}_e, \vec{\omega}_p$) over a surface terminating on the disclination line in a discrete setting, even though a smooth elastic curvature field $\boldsymbol{\kappa}_e$ exists in this region. The strength of disclinations is characterized by their Frank vector $\boldsymbol{\Omega}$, which represents the magnitude and direction of the rotational discontinuity $\boldsymbol{\Omega} = \llbracket\vec{\omega}_e\rrbracket$ over a closed circuit encircling the disclination line. In deWit's continuous setting (deWit, 1970), also adopted in the present paper, the smooth elastic curvature field is irrotational outside the disclination core region, and the disclination density tensor is defined as the curl of this field inside the core, of non-zero volume:

$$\boldsymbol{\theta} = \mathbf{curl}\,\boldsymbol{\kappa}_e. \tag{18}$$

The Frank vector is then obtained by integrating the disclination density tensor field over appropriate surface patches S:

$$\boldsymbol{\Omega} = \int_S \boldsymbol{\theta} \cdot \mathbf{n}\,dS. \tag{19}$$

Acharya and Fressengeas (2012) adopted a similar approach in introducing g-disclinations, as shown in Fig. 1. The g-disclination concept goes beyond the Volterra construct, in the sense that the elastic distortion field now has a discontinuity $\llbracket\mathbf{U}_e\rrbracket$ along a surface terminating at the g-disclination line (Fig. 1), whereas the elastic 2-distortion tensor field $\mathbf{G}_e$ is still smooth in the non-simply connected region excluding the g-disclination line. As already mentioned, this surface of discontinuity is referred as to a phase boundary.

The strength $\boldsymbol{\Pi}$ of the g-disclination is defined as the jump in the elastic distortion tensor field across the interphase: $\boldsymbol{\Pi} = \llbracket\mathbf{U}_e\rrbracket$. In a continuous setting, the elastic 2-distortion field is point-wise irrotational in the defect free volume of the body. Its curl in the defected part provides for the definition of the third order g-disclination density tensor field $\boldsymbol{\pi}$:

$$\boldsymbol{\pi} = \mathbf{curl}\,\mathbf{G}_e, \tag{20}$$

and the integration of the latter over an appropriate surface patch yields the jump of the elastic distortion tensor field:

$$\boldsymbol{\Pi} = \int_S \boldsymbol{\pi}.\mathbf{n}\,dS \tag{21}$$

When, as a special case, the discontinuity in the elastic strain field vanishes, while a discontinuity $\llbracket\vec{\omega}_e\rrbracket$ in the elastic rotation field is persisting, the g-disclinations reduce to standard disclinations, as illustrated in Fig. 2. In the context of a discontinuous elastic distortion field, the dislocation density tensor $\boldsymbol{\alpha}$ needs to be re-defined by the rotation of the 2-distortion tensor (Acharya and Fressengeas, 2012):

$$\boldsymbol{\alpha} = -\mathbf{G}_e : \mathbf{X} \tag{22}$$

instead of Eq. (16), because $\mathbf{U}_e$ does not have anymore the continuity required in this relation (Acharya and Fressengeas, 2012). If, as is customary in dislocation theory, $\mathbf{U}_e$ does not feature a discontinuity, $\mathbf{G}_e = \mathbf{grad}\,\mathbf{U}_e$ and, using the identity (8), it is straightforward to show that Eq. (22) reduces to Eq. (16).

3.3. Stokes–Helmholtz decomposition and Poisson-type equations

Invoking the Stokes–Helmholtz orthogonal decomposition of the square-integrable elastic 2-distortion tensor field $\mathbf{G}_e$ with square-integrable first order derivatives (see for example Jiang,
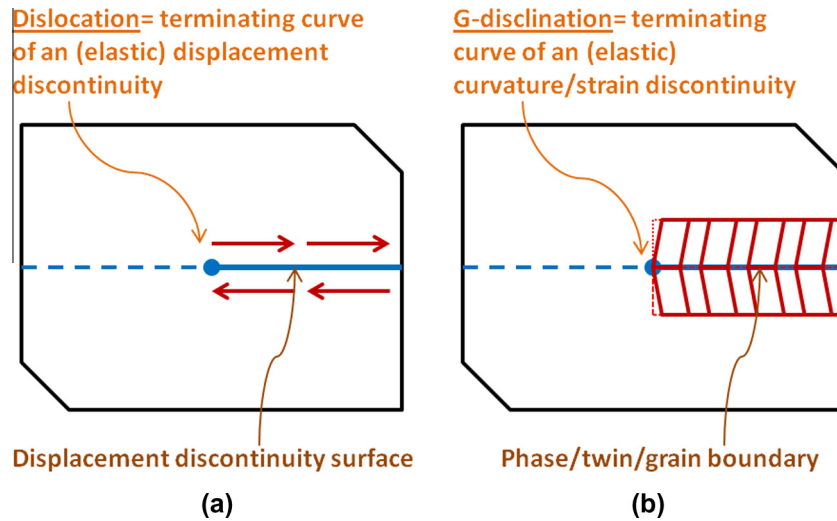
Fig. 1. Cross sectional view of the two types of introduced straight line defects in the present paper: dislocation (a) seen as the terminating curve of the surface of elastic displacement discontinuity (the arrows with reverse directions along the displacement discontinuity surface describe different displacement directions), g-disclination (b) seen as the terminating curve of the surface of elastic curvature/strain discontinuity as introduced in Acharya and Fressengeas (2012) (the differently inclined parallel lines in the vicinity of the distortion discontinuity surface describe different elastic curvatures/strains, like different shears for example). Further examples are provided in Fig. 2.
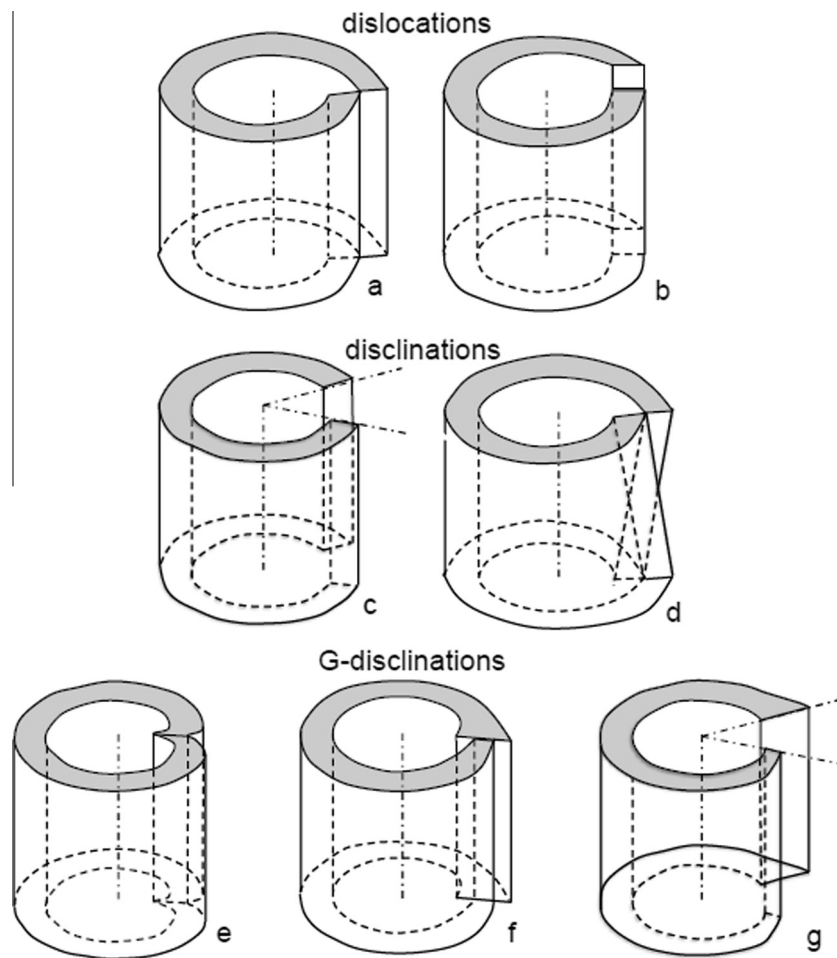

Fig. 2. Examples of Volterra, 1907's dislocations and disclinations (a-d): edge (a), screw (b) dislocations (displacement discontinuities), wedge (c), twist (d) standard disclinations (rotation discontinuities), and, illustration of g-disclinations (e-g) (Acharya and Fressengeas, 2012) due to shear (e), stretch (f) and stretch + rotation (g) discontinuities. The considered standard disclinations are particular cases of g-disclinations and case (g) is equivalent to (c)+(f). The axis of the cylinders represents the terminating curve of the surfaces of discontinuity introduced in Fig. 1. Note that we do not cut out the inner cylinder from the investigated domain in order to leave a multiply-connected but compatible body, as in theories of discrete defects. In the present elasto-static Field Dislocation/G-Disclination Mechanics theory (FDGDM), the defect density is continuously distributed in a simply-connected but incompatible core region.

1998, Theorem 5.8), there exist unique tensor fields $\boldsymbol{\chi}$ and $\mathbf{Z}$ (up to a constant for the latter, both fields being square-integrable as well as their derivatives to second order) such that $\mathbf{G}_e$ writes as the sum:

$$\mathbf{G}_e = \mathbf{curl}\,\boldsymbol{\chi} + \mathbf{grad}\,\mathbf{Z}. \tag{23}$$

with the orthogonality condition $\int_V \mathbf{curl}\,\boldsymbol{\chi} : \mathbf{grad}\,\mathbf{Z}\,dv = 0$. Thus, taking the curl of $\mathbf{G}_e$ in Eq. (23) extracts $\mathbf{curl}\,\boldsymbol{\chi}$ and discards $\mathbf{grad}\,\mathbf{Z}$ (curl-free), whereas taking its divergence extracts $\mathbf{grad}\,\mathbf{Z}$ and eliminates $\mathbf{curl}\,\boldsymbol{\chi}$ (divergence-free). Therefore, Eq. (20) involves only $\mathbf{curl}\,\boldsymbol{\chi}$, which we will identify below as the incompatible part $\mathbf{G}_e^\perp$ of $\mathbf{G}_e$:

$$\mathbf{curl}\,\mathbf{G}_e^\perp = \mathbf{curl}\,\mathbf{curl}\,\boldsymbol{\chi} = \boldsymbol{\pi}. \tag{24}$$

Similarly, $\mathbf{grad}\,\mathbf{Z}$ will be the compatible part $\mathbf{G}_e^\parallel$ of the elastic 2-distortion $\mathbf{G}_e$, and $\mathbf{Z}$ will be the elastic distortion $\mathbf{U}_e$, up to a constant. To ensure correctness of this identification, $\mathbf{G}_e^\perp$ must vanish identically throughout the body when $\boldsymbol{\pi} = 0$. In this aim, following Jiang (1998), Acharya (2001) and Acharya and Fressengeas (2012), Eq. (24) is augmented with the conditions:

$$\mathbf{div}\,\mathbf{G}_e^\perp = 0 \quad \text{in } V \tag{25}$$

$$\mathbf{G}_e^\perp \cdot \mathbf{n} = 0 \quad \text{on } \partial V \tag{26}$$

with unit normal $\mathbf{n}$ on ∂V. Then taking the curl of Eq. (20) and using the complementary condition (25), it follows that:

$$\mathbf{curl}\,\mathbf{curl}\,\mathbf{G}_e^\perp = \mathbf{grad}\,\mathbf{div}\,\mathbf{G}_e^\perp - \mathbf{div}\,\mathbf{grad}\,\mathbf{G}_e^\perp = -\mathbf{div}\,\mathbf{grad}\,\mathbf{G}_e^\perp$$
$$= \mathbf{curl}\,\boldsymbol{\pi} \tag{27}$$

Hence, $\mathbf{G}_e^\perp$ satisfies the Poisson-type equation

$$\mathbf{div}\,\mathbf{grad}\,\mathbf{G}_e^\perp = -\mathbf{curl}\,\boldsymbol{\pi} \quad \text{in } V \tag{28}$$

$$\mathbf{G}_e^\perp \cdot \mathbf{n} = 0 \quad \text{on } \partial V. \tag{29}$$

In component form, Eq. (28) reads

$$G_{ijk,ll}^{e,\perp} = -e_{klm}\pi_{ijm,l} \tag{30}$$

As a consequence, the field of incompatible elastic 2-distortion $\mathbf{G}_e^\perp$ is uniquely determined once the g-disclination density field $\boldsymbol{\pi}$ is prescribed. In particular, it vanishes uniformly when $\boldsymbol{\pi} = 0$. Using Eqs. (22), (8) and (23), and the fact that $\mathbf{Z}$ is $\mathbf{U}_e$, up to a constant, the dislocation density tensor can therefore be written as:

$$\boldsymbol{\alpha} = -\mathbf{G}_e^\perp : \mathbf{X} - \mathbf{grad}\,\mathbf{U}_e : \mathbf{X} = \mathbf{curl}\,\mathbf{U}_e - \mathbf{G}_e^\perp : \mathbf{X} \tag{31}$$

In turn, the Stokes–Helmholtz decomposition of the elastic distortion $\mathbf{U}_e$ can be used to separate its compatible part, $\mathbf{U}_e^\parallel$, from its incompatible part, $\mathbf{U}_e^\perp$:

$$\mathbf{U}_e = \mathbf{U}_e^\perp + \mathbf{U}_e^\parallel = \mathbf{curl}\,\boldsymbol{\psi} + \mathbf{grad}\,\mathbf{w} \tag{32}$$

and to ensure uniqueness of the latter through the solution of a Poisson-type equation. This decomposition for $\mathbf{U}_e$ was also recently invoked by Brenner et al. (2014) in their spectral approach for field dislocation mechanics to prove the uniqueness of stress and elastic distortion. In Eq. (32), $\mathbf{U}_e^\parallel = \mathbf{grad}\,\mathbf{w}$ again belongs to the null-space of the curl operator since $\mathbf{curl}\,\mathbf{grad}\,\mathbf{w} = 0$, while $\mathbf{U}_e^\perp = \mathbf{curl}\,\boldsymbol{\psi}$ must additionally satisfy the conditions:

$$\mathbf{div}\,\mathbf{U}_e^\perp = 0 \quad \text{in } V \tag{33}$$

$$\mathbf{U}_e^\perp \cdot \mathbf{n} = 0 \quad \text{on } \partial V. \tag{34}$$

Invoking the identity $\mathbf{curl}\,\mathbf{curl}\,\mathbf{U}_e^\perp = \mathbf{grad}\,\mathbf{div}\,\mathbf{U}_e^\perp - \mathbf{div}\,\mathbf{grad}\,\mathbf{U}_e^\perp$, taking the curl of Eq. (31) and using Eq. (33) then leads to the Poisson-type equation:

$$\mathbf{div}\,\mathbf{grad}\,\mathbf{U}_e^\perp = -\mathbf{curl}\,(\boldsymbol{\alpha} + \mathbf{G}_e^\perp : \mathbf{X}) \quad \text{in } V \tag{35}$$

$$\mathbf{U}_e^\perp \cdot \mathbf{n} = 0 \quad \text{on } \partial V. \tag{36}$$

In component form, Eq. (35) reads

$$U_{ij,kk}^{e,\perp} = -e_{jkl}\alpha_{il,k} - (G_{ijk}^{e,\perp} - G_{ikj}^{e,\perp})_{,k} \tag{37}$$

Hence, $\mathbf{U}_e^\perp$ is uniquely determined once the dislocation and g-disclination density fields $(\boldsymbol{\alpha}, \boldsymbol{\pi})$ are prescribed. In particular, it vanishes uniformly in V when $\boldsymbol{\alpha} = 0$ and $\boldsymbol{\pi} = 0$. Eq. (28), and Eq. (35) will be transformed in the Fourier space in Section 4, and solved using the Fast Fourier Transform (FFT) method based on a discrete Fourier transforms formulation (see Section 5).

3.4. Navier-type equations for compatible distortion fields

The elasto-static field equations (14), (15) and (32) can be rewritten in the form of a partial differential equation of Navier-type in V:

$$\mathbf{div}\,\mathbf{C} : \mathbf{U}_e^{\parallel,sym} + \mathbf{f}^\perp = 0, \tag{38}$$

where $\mathbf{U}_e^\parallel = \mathbf{grad}\,\mathbf{w}$, and the volumetric force density $\mathbf{f}^\perp = \mathbf{div}\,\mathbf{C} : \mathbf{U}_e^{\perp,sym}$ reflects the incompatibility arising from the presence of defects. This equation is appended by boundary conditions on $\mathbf{U}_e^\parallel$ along ∂V:

$$\mathbf{w} = 0 \quad \text{on } \partial V_u \quad \text{and}$$

$$\mathbf{C} : \mathbf{U}_e^{\parallel,sym} \cdot \mathbf{n} = \mathbf{t}^d - \mathbf{C} : \mathbf{U}_e^{\perp,sym} \cdot \mathbf{n} \quad \text{on } \partial V_t. \tag{39}$$

The Navier equation (38) and boundary conditions (39) set a standard elasticity problem for the unknown field $\mathbf{U}_e^\parallel$, which can therefore be determined uniquely. The volumetric force density $\mathbf{f}^\perp$ is first determined by solving the Poisson equations (28) and (35) for $\mathbf{G}_e^\perp$ and $\mathbf{U}_e^\perp$, after defect density fields $(\boldsymbol{\alpha}, \boldsymbol{\pi})$ have been initially prescribed.

Assuming a homogeneous reference medium with linear elastic moduli $\mathbf{C}^0$, such that $\mathbf{C} = \mathbf{C}^0 + \delta\mathbf{C}$, Eq. (38) yields, in component form:

$$C_{ijkl}^0 w_{k,lj} + C_{ijkl}^0 \varepsilon_{kl,j}^{e,\perp} + \tau_{ij,j} = 0. \tag{40}$$

In this equation, $\boldsymbol{\tau} = \delta\mathbf{C} : \mathbf{U}_e^{\perp,sym} + \delta\mathbf{C} : \mathbf{U}_e^{\parallel,sym} = \delta\mathbf{C} : \boldsymbol{\varepsilon}_e$ is the classic "stress polarization tensor field" for heterogeneous elasticity (Willis, 1981). Since the latter contains the unknown compatible elastic strain, Eq. (40) is solved through an integral Lippmann–Schwinger-type equation. The general formal field solution in the case of heterogeneous elasticity is given by a power series (Vinogradov and Milton, 2008; Brenner et al., 2014).

In the particular case of homogeneous elasticity described by the elastic moduli C_{ijkl}^0, the polarization tensor field vanishes and Eq. (40) reduces to

$$C_{ijkl}^0 w_{k,lj} + C_{ijkl}^0 \varepsilon_{kl,j}^{e,\perp} = 0. \tag{41}$$

For isotropic elasticity: $C_{ijkl}^0 = \lambda\delta_{ij}\delta_{kl} + \mu(\delta_{ik}\delta_{jl} + \delta_{il}\delta_{jk})$, and Eq. (41) yields

$$\mu w_{i,kk} + (\lambda + \mu)w_{k,ki} + \lambda U_{kk,i}^{e,\perp} + \mu\left(U_{ik,k}^{e,\perp} + U_{ki,k}^{e,\perp}\right) = 0, \tag{42}$$

where μ and λ are respectively the shear modulus and Lamé constant of the material.

4. Spectral method

4.1. Solution of Poisson-type equations in Fourier space

The previous Poisson and Navier-type equations can be solved using the Fourier Transform method. Indeed, unknown periodic vector field $\mathbf{w}(\boldsymbol{x})$ and tensor field $\mathbf{U}_e(\boldsymbol{x})$ can be solved by using the spectral method based on Fourier transforms to derive later on the stresses, elastic rotations etc. in the Fourier space. Then,

the elastic fields are estimated in the real space using the inverse Fourier Transform. The FFT algorithm is well suited for periodic media. It will be developed in Section 5 to estimate the discrete Fourier transforms on FFT grids.

In the Fourier space, let ξ be the Fourier vector of magnitude $\xi = \sqrt{\xi \cdot \xi}$ and components ξ_i in a cartesian coordinate system in a general three-dimensional setting. The complex imaginary number is denoted i and defined as $i = \sqrt{-1}$.

Let $\widetilde{\boldsymbol{\alpha}}(\boldsymbol{\xi})$, $\widetilde{\mathbf{U}}_e^{\perp}(\boldsymbol{\xi})$, $\widetilde{\boldsymbol{\pi}}(\boldsymbol{\xi})$ and $\widetilde{\mathbf{G}}_e^{\perp}(\boldsymbol{\xi})$ be the continuous Fourier transforms of $\boldsymbol{\alpha}(\boldsymbol{x})$, $\mathbf{U}_e^{\perp}(\boldsymbol{x})$, $\boldsymbol{\pi}(\boldsymbol{x})$ and $\mathbf{G}_e^{\perp}(\boldsymbol{x})$. Then, the Poisson-type equations: Eqs. (28) and (35) are solved using the differentiation theorem in Fourier space. Using component notations, Eqs. (28) and (29) write in the Fourier space

$$\widetilde{G}_{ijk}^{e,\perp}(\boldsymbol{\xi}) = \frac{i}{\xi^2}\xi_l e_{klm}\widetilde{\pi}_{ijm}(\boldsymbol{\xi}) \quad \forall \boldsymbol{\xi} \neq \mathbf{0}$$
$$\widetilde{G}_{ijk}^{e,\perp}(\mathbf{0}) = \mathbf{0}$$
(43)

and Eqs. (36) and (37) yield in the Fourier space

$$\widetilde{U}_{ij}^{e,\perp}(\boldsymbol{\xi}) = \frac{i}{\xi^2}\xi_k\left(e_{jkl}\widetilde{\alpha}_{il}(\boldsymbol{\xi}) + \widetilde{G}_{ijk}^{e,\perp}(\boldsymbol{\xi}) - \widetilde{G}_{ikj}^{e,\perp}(\boldsymbol{\xi})\right) \quad \forall \boldsymbol{\xi} \neq \mathbf{0}$$
$$\widetilde{U}_{ij}^{e,\perp}(\mathbf{0}) = \mathbf{0}$$
(44)

If only dislocation-type defects are present, Eq. (44) reduces to the first term, which was also very recently reported in Brenner et al. (2014).

4.2. Solution of Navier-type equation in Fourier space

Let $\widetilde{\mathbf{w}}(\boldsymbol{\xi})$ and $\widetilde{\mathbf{U}}_e^{\parallel}(\boldsymbol{\xi})$ be the continuous Fourier transform of $\mathbf{w}(\boldsymbol{x})$ and $\mathbf{U}_e^{\parallel}(\boldsymbol{x})$. Then, the Fourier transform of the Navier-type equation (Eq. (40)) yields

$$C_{ijkl}^0\xi_l\xi_j\widetilde{w}_k(\boldsymbol{\xi}) = iC_{ijkl}^0\xi_j\widetilde{U}_{kl}^{e,\perp}(\boldsymbol{\xi}) + i\xi_j\widetilde{\tau}_{ij}(\boldsymbol{\xi})$$
(45)

Furthermore, the compatible elastic distortion $\widetilde{\mathbf{U}}_e^{\parallel}(\boldsymbol{\xi})$ is obtained in the Fourier space from the differentiation rule

$$\widetilde{U}_{ij}^{e,\parallel}(\boldsymbol{\xi}) = i\xi_j\widetilde{w}_i(\boldsymbol{\xi})$$
(46)

Thus, combining Eqs. (45) and (46) yields $\widetilde{U}_{ij}^{e,\parallel}(\boldsymbol{\xi})$ as the solution of an implicit algebraic equation in the Fourier space

$$\widetilde{U}_{ij}^{e,\parallel}(\boldsymbol{\xi}) = -\xi_l\xi_j\widetilde{G}_{ik}(\boldsymbol{\xi})\left(\delta C_{klmn}\widetilde{U}_{mn}^{e,\parallel}(\boldsymbol{\xi}) + C_{klmn}\widetilde{U}_{mn}^{e,\perp}(\boldsymbol{\xi})\right)$$
(47)

where $\widetilde{\mathbf{G}}(\boldsymbol{\xi})$ is the Fourier transform of the Green tensor $\mathbf{G}$ associated with the homogeneous elastic moduli $\mathbf{C}^0$ and determined as follows

$$\widetilde{G}_{ik}(\boldsymbol{\xi}) = \frac{N_{ik}(\boldsymbol{\xi})}{D(\boldsymbol{\xi})} \forall \boldsymbol{\xi} \neq \mathbf{0}$$
$$\widetilde{G}_{ik}(\mathbf{0}) = \mathbf{0}$$
(48)

where $N_{ik}(\boldsymbol{\xi})$ and $D(\boldsymbol{\xi})$ are respectively the co-factor matrix and the determinant of $K_{ik}(\boldsymbol{\xi}) = C_{ijkl}^0\xi_l\xi_j$, the so-called "acoustic tensor" (Mura, 1987). This implicit equation to determine $\widetilde{U}_{ij}^{e,\parallel}(\boldsymbol{\xi})$ is generally solved numerically in the Fourier space using different iterative schemes. The major ones are the "basic scheme" (Moulinec and Suquet, 1998; Lebensohn, 2001), the "accelerated scheme" (Eyre and Milton, 1999; Vinogradov and Milton, 2008) and the " augmented Lagrangian scheme" (Michel et al., 2001; Lebensohn et al., 2012). In the case of the basic iterative scheme, convergence is based on fulfilment of stress equilibrium in the Fourier space (Moulinec and Suquet, 1998; Lebensohn, 2001). The convergence rate depends on the elasticity moduli contrast and on the choice of the initial reference medium $\mathbf{C}^0$. Different approaches were developed to improve this convergence rate for strong elastic contrasts between the phases (Eyre and Milton, 1999; Michel et al.,

2001; Vinogradov and Milton, 2008; Brisard and Dormieux, 2010; Monchiet and Bonnet, 2013).

In the following, the solution of the Navier equation (40) in Fourier space will be restricted to linear homogeneous elastic media with elastic moduli $\mathbf{C}^0$ where no iterative solution is needed (no stress polarization field). In the case of homogeneous elasticity, i.e. $\mathbf{C} = \mathbf{C}^0$, the equation becomes explicit

$$\widetilde{w}_i(\boldsymbol{\xi}) = iC_{klmn}^0\xi_l\widetilde{G}_{ik}(\boldsymbol{\xi})\widetilde{U}_{mn}^{e,\perp}(\boldsymbol{\xi})$$
$$\widetilde{U}_{ij}^{e,\parallel}(\boldsymbol{\xi}) = -C_{klmn}^0\xi_l\xi_j\widetilde{G}_{ik}(\boldsymbol{\xi})\widetilde{U}_{mn}^{e,\perp}(\boldsymbol{\xi})$$
(49)

In the case of isotropic elasticity, i.e. $C_{ijkl}^0 = \lambda\delta_{ij}\delta_{kl} + \mu(\delta_{ik}\delta_{jl} + \delta_{il}\delta_{jk})$, the expression of $\widetilde{G}_{ik}(\boldsymbol{\xi})$ is given by Mura (1987) $\forall \boldsymbol{\xi} \neq \mathbf{0}$

$$\widetilde{G}_{ik}(\boldsymbol{\xi}) = \frac{(\lambda + 2\mu)\delta_{ik}\xi^2 - (\lambda + \mu)\xi_i\xi_k}{\mu(\lambda + 2\mu)\xi^4}$$
(50)

Using Eq. (50), Eq. (49) simplifies into

$$\widetilde{w}_i(\boldsymbol{\xi}) = i(\lambda + 2\mu)^{-1}\xi^{-4}$$
$$\times \left[\lambda\xi_i\xi^2\widetilde{U}_{pp}^{e,\perp}(\boldsymbol{\xi}) + (\lambda + 2\mu)\xi_l\xi^2\left(\widetilde{U}_{il}^{e,\perp}(\boldsymbol{\xi}) + \widetilde{U}_{li}^{e,\perp}(\boldsymbol{\xi})\right)\right.$$
$$\left. -(\lambda + \mu)\xi_i\xi_k\xi_l\left(\widetilde{U}_{kl}^{e,\perp}(\boldsymbol{\xi}) + \widetilde{U}_{lk}^{e,\perp}(\boldsymbol{\xi})\right)\right]$$

$$\widetilde{U}_{ij}^{e,\parallel}(\boldsymbol{\xi}) = -(\lambda + 2\mu)^{-1}\xi^{-4}$$
$$\times \left[\lambda\xi_i\xi_j\xi^2\widetilde{U}_{pp}^{e,\perp}(\boldsymbol{\xi}) + (\lambda + 2\mu)\xi_l\xi_j\xi^2\left(\widetilde{U}_{il}^{e,\perp}(\boldsymbol{\xi}) + \widetilde{U}_{li}^{e,\perp}(\boldsymbol{\xi})\right)\right.$$
$$\left. -(\lambda + \mu)\xi_i\xi_j\xi_k\xi_l\left(\widetilde{U}_{kl}^{e,\perp}(\boldsymbol{\xi}) + \widetilde{U}_{lk}^{e,\perp}(\boldsymbol{\xi})\right)\right]$$
(51)

4.3. Stress field

Knowing $\widetilde{\mathbf{U}}_e^{\perp}(\boldsymbol{\xi})$ and $\widetilde{\mathbf{U}}_e^{\parallel}(\boldsymbol{\xi})$, the (total) elastic distortion in the Fourier space yields

$$\widetilde{U}_{ij}^e = \widetilde{U}_{ij}^{e,\perp} + \widetilde{U}_{ij}^{e,\parallel}$$
(52)

The stress $\widetilde{\mathbf{T}}(\boldsymbol{\xi})$ is obtained in component form as:

$$\widetilde{T}_{ij}(\boldsymbol{\xi}) = C_{ijkl}^0\widetilde{\varepsilon}_{kl}^e(\boldsymbol{\xi}) \forall \boldsymbol{\xi} \neq \mathbf{0}$$
$$\widetilde{T}_{ij}(\mathbf{0}) = \overline{T}_{ij}$$
(53)

where $\widetilde{\varepsilon}_{ij}^e = \frac{1}{2}\left(\widetilde{U}_{ij}^e + \widetilde{U}_{ji}^e\right)$ and $\overline{T}_{ij}$ is the macroscopic stress which is also the spatial average of T_{ij} over the periodic unit cell (using spatial average theorem).

Using Eq. (49) together with Eq. (53) yields

$$\widetilde{T}_{ij}(\boldsymbol{\xi}) = \left(I_{ijmn} - C_{ijkl}^0\widetilde{\Gamma}_{klmn}(\boldsymbol{\xi})\right)C_{mnpq}^0\widetilde{U}_{pq}^{e,\perp}(\boldsymbol{\xi}) \forall \boldsymbol{\xi} \neq \mathbf{0}$$
$$\widetilde{T}_{ij}(\mathbf{0}) = \overline{T}_{ij}$$
(54)

where $\widetilde{\Gamma}_{klmn}(\boldsymbol{\xi})$ is the Fourier transform of the modified Green operator introduced by Kröner (1989) and defined in the Fourier space as

$$\widetilde{\Gamma}_{ijkl}(\boldsymbol{\xi}) = \frac{1}{2}\left(\widetilde{G}_{ik}(\boldsymbol{\xi})\xi_l\xi_j + \widetilde{G}_{jk}(\boldsymbol{\xi})\xi_l\xi_i\right)$$
(55)

In the case of isotropic elasticity, the expression of $\widetilde{\Gamma}_{klmn}(\boldsymbol{\xi})$ is given from Eq. (50) by

$$\widetilde{\Gamma}_{klmn}(\boldsymbol{\xi}) = (4\mu)^{-1}\xi^{-2}(\delta_{km}\xi_n\xi_l + \delta_{kn}\xi_m\xi_l + \delta_{lm}\xi_k\xi_n + \delta_{ln}\xi_k\xi_m)$$
$$- \frac{(\lambda + \mu)}{\mu(\lambda + 2\mu)}\frac{\xi_k\xi_l\xi_m\xi_n}{\xi^4}$$
(56)

Then, the inverse Fourier transforms of $\widetilde{\mathbf{T}}(\boldsymbol{\xi})$ is numerically computed using the FFT algorithm, while inverse FFT allows finding

T on the discretized periodic unit cell. Other elastic fields, such as elastic rotations, curvatures and strains can also be derived.

5. Fast Fourier Transform numerical implementation

5.1. Discrete Fourier Transforms and FFT

The continuous field equations in the Fourier space (see Section 4 for the derivations of Poisson and Navier-type equations) are now solved by 2D discrete Fourier transforms with the Fast Fourier Transform (FFT) algorithm. Thus, periodicity is assumed for the distribution of dislocation or g-disclination densities (i.e. $\boldsymbol{\alpha}$ or $\boldsymbol{\pi}$), with spatial periods T_1 and T_2 in the x_1 and x_2 directions, respectively. The periodic representative volume element (RVE) or unit cell is discretized by a regular rectangular grid with $N_1 \times N_2$ pixels with position vector $\boldsymbol{x} = ((i-1)\delta_1, (j-1)\delta_2)$, where $i = 1 \to N_1$, $j = 1 \to N_2$ and δ_1, δ_2 are the pixel sizes in the x_1 and x_2 directions. The total number of FFT grid points is $N_{tot} = N_1 \times N_2$. Here, the FFTW package of Matlab is used to compute discrete Fourier transforms (FFTW, 1998; Matlab, 2012). The discrete FFT of a given spatial function f is $\widehat{f} = \text{FFT}(f)$. It inverse Fourier transform is $f = \text{FFT}^{-1}(\widehat{f})$. They write with the Matlab FFT convention:

$$\widehat{f}(k,l) = \sum_{i=1}^{N_1}\sum_{j=1}^{N_2} f(i,j)\exp\left(-2\pi i\left(\frac{(i-1)(k-1)}{N_1}+\frac{(j-1)(l-1)}{N_2}\right)\right) \tag{57}$$

and

$$f(i,j) = \frac{1}{N_{tot}}\sum_{k=1}^{N_1}\sum_{l=1}^{N_2} \widehat{f}(k,l)\exp\left(+2\pi i\left(\frac{(i-1)(k-1)}{N_1}+\frac{(j-1)(l-1)}{N_2}\right)\right) \tag{58}$$

It should be pointed out that Eqs. (57) and (58) are finite sums which can be determined exactly by FFT for periodic RVE, but not approximations of the continuous Fourier transforms introduced in Section 4.

5.2. Differentiation rules

Here, the following differentiation rules are used for first and second order partial derivatives onto the discrete grid based on 9-pixel approximation of partial derivatives using centered differences (Press et al., 2002):

$$\frac{\partial f(i,j)}{\partial x_1} = \frac{f(i+1,j)-f(i-1,j)}{2\delta_1} \tag{59}$$

$$\frac{\partial f(i,j)}{\partial x_2} = \frac{f(i,j+1)-f(i,j-1)}{2\delta_2} \tag{60}$$

$$\frac{\partial^2 f(i,j)}{\partial x_1^2} = \frac{f(i+1,j)-2f(i,j)+f(i-1,j)}{\delta_1^2} \tag{61}$$

$$\frac{\partial^2 f(i,j)}{\partial x_2^2} = \frac{f(i,j+1)-2f(i,j)+f(i,j-1)}{\delta_2^2} \tag{62}$$

$$\frac{\partial^2 f(i,j)}{\partial x_1 \partial x_2} = \frac{f(i+1,j+1)-f(i+1,j-1)-f(i-1,j+1)+f(i-1,j-1)}{4\delta_1\delta_2} \tag{63}$$

Using Eqs. (57), (58) and (59)–(63), the corresponding multipliers in the Fourier space between continuous and discrete Fourier transforms for partial derivatives are the following:

$$i\xi_1 \leftrightarrow \frac{i}{\delta_1}\sin\left(\frac{2\pi(k-1)}{N_1}\right) \tag{64}$$

$$i\xi_2 \leftrightarrow \frac{i}{\delta_2}\sin\left(\frac{2\pi(l-1)}{N_2}\right) \tag{65}$$

$$-\xi_1^2 \leftrightarrow \frac{2}{\delta_1^2}\left(\cos\left(\frac{2\pi(k-1)}{N_1}\right)-1\right) \tag{66}$$

$$-\xi_2^2 \leftrightarrow \frac{2}{\delta_2^2}\left(\cos\left(\frac{2\pi(l-1)}{N_2}\right)-1\right) \tag{67}$$

$$-\xi_1\xi_2 \leftrightarrow \frac{1}{2\delta_1\delta_2}\left[\cos\left(2\pi\left(\frac{(k-1)}{N_1}+\frac{(l-1)}{N_2}\right)\right)-\cos\left(2\pi\left(\frac{(k-1)}{N_1}-\frac{(l-1)}{N_2}\right)\right)\right] \tag{68}$$

In the next section, Eqs. (64)–(68) will be applied to obtain the incompatible (second order $\mathbf{G}_e^\perp$ and first order $\mathbf{U}_e^\perp$) and compatible ($\mathbf{U}_e^\parallel$) field solutions in the discretized Fourier space using 2D FFT square grids with pixel size $\delta_1 = \delta_2 = \delta$. The useful detailed calculations of spatial derivatives in the discrete Fourier space are fully reported in the Appendix A (for incompatible fields) and in the Appendix B (for compatible fields). Such "intrinsic" discrete Fourier transform methodology was first highlighted in Müller (1996), Müller (1998) and Dreyer et al. (1999). The numerical classic FFT approach first developed by Moulinec and Suquet (1994), Moulinec and Suquet (1998) and recently adapted for field dislocation mechanics by Brenner et al. (2014) is based on a linear Taylor expansion sometimes called "acoustic limit" of the present intrinsic DFT formulation. It is noteworthy that higher order pixel approximations may also be developed (Neumann et al., 2002) to further refine the FFT analysis. As will be shown in the Section 6 of the present paper, the 9-pixel centered finite difference approximation is sufficient to give accurate results for strong gradients of stress/strain fields of pure screw/edge dislocations and pure g-disclinations near their cores in comparison with existing analytical solutions. In Section 7, we will discuss how the present FFT method based on intrinsic discrete Fourier transforms avoids spurious Gibbs oscillations occurring when using classic FFT techniques based on continuous Fourier transforms.

6. Applications to infinite straight dislocations and g-disclinations

6.1. Materials and numerical data

In the forthcoming applications, the dislocation and g-disclination cores are prescribed using different functions: either singular functions using Riemann-Graves operator and algebra (Acharya, 2001), or regular Gaussian functions like those used in phase field approaches for dislocations (Hu and Chen, 2001). 2D FFT $N \times N$ square grids with $\delta_1 = \delta_2 = \delta, N_1 = N_2 = N$ and $N_{tot} = N^2$ will be used. It will be shown that Gaussian functions with low standard deviation are very good candidates to regularize dislocation cores in the present FFT-FDGDM (Field Dislocation and G-Disclination Mechanics) framework, by comparison with other possible numerical schemes. In this section, the FFT grids will be set to 1024×1024 pixels (for dislocations) or 2048×2048 pixels (for g-disclinations) and two different pixel sizes: $\delta = 0.05b$ (for dislocations) and $\delta = 0.1b$ (for g-disclinations) where b is the magnitude of the Burgers vector. The isotropic elastic constants of aluminium (Al) will be used for the simulations: E = 62780 MPa, $v = 0.3647$. The Burgers vector magnitude is set to $b = 4.05 \times 10^{-10}$ m. These constants were already used by Roy and Acharya (2005) in their finite element simulations. In the simulations, the dislocation core radius is chosen to be $r_0 = 0.6b$.

In the following, stresses for both pure screw and edge dislocations (see Fig. 2) and straight g-disclinations (see Fig. 1) will be computed to assess the present numerical spectral method. Furthermore, elastic rotations induced by a screw dislocation and elastic curvatures induced by a pure straight wedge disclination will be reported. The numerical FFT results will be compared to

analytical formulations reported in Hirth and Lothe (1982), Acharya (2001), deWit (1973) and Romanov and Vladimirov (1992). For a single screw dislocation with a Gaussian dislocation density distribution, the results obtained by FFT will be compared to that obtained by FEM for identical periodic boundary value problem and mesh/pixel sizes.

6.2. Dislocations

6.2.1. Single screw dislocation

A single infinitely straight screw dislocation is first considered. The dislocation line lies along the $\mathbf{e}_3$ axis with Burgers vector $\mathbf{b} = b\mathbf{e}_3$ and unit line vector $\mathbf{t} = \mathbf{e}_3$. Thus, the only non-zero component of the dislocation density tensor is $\alpha_{33}(\mathbf{x})$. A spatial distribution of the latter will be prescribed in the center of the periodic unit cell. For this dislocation density, Eq. (37) reduces to two independent Poisson-type equations

$$U_{31,11}^{e,\perp} + U_{31,22}^{e,\perp} = -\alpha_{33,2} \tag{69}$$

$$U_{32,11}^{e,\perp} + U_{32,11}^{e,\perp} = \alpha_{33,1} \tag{70}$$

where $U_{31}^{e,\perp}$ and $U_{32}^{e,\perp}$ are the only non zero incompatible elastic distortions.

The solution algorithm is now described. First, the FFT of α_{33} is computed, i.e. $\widehat{\alpha_{33}}$ using Eq. (57). Second, the solutions of Poisson-type equations for $\widehat{U_{32}^{e,\perp}}$ (Eq. (70)) and $\widehat{U_{31}^{e,\perp}}$ (Eq. (69)) are given in the Fourier space using the FFT algorithm (see Appendix A, Eqs. (A.1)–(A.3)). Inverse FFT (Eq. (58)) is used to compute $U_{32}^{e,\perp}$ and $U_{31}^{e,\perp}$. In the case of infinitely straight screw dislocation in a homogeneous linear isotropic elastic medium, which is a particular and remarkable case, the only non zero shear stresses are simply computed from the non zero incompatible elastic distortions as follows

$$T_{23} = T_{32} = \mu U_{32}^{e,\perp} \tag{71}$$

$$T_{13} = T_{31} = \mu U_{31}^{e,\perp} \tag{72}$$

Indeed, by using Eq. (33), it is easy to see that these shear stresses satisfy balance of momentum, without the need of compatible elastic distortions. Stress self-equilibrium is checked in both Fourier and real spaces. Other elastic fields can be determined in the real space, such as the following non zero elastic rotation components

$$\omega_{32}^e = -\omega_{23}^e = \frac{U_{32}^{e,\perp}}{2} \tag{73}$$

$$\omega_{31}^e = -\omega_{13}^e = \frac{U_{31}^{e,\perp}}{2} \tag{74}$$

The assessment of the numerical spectral method is first conducted using an analytical solution obtained with the Riemann-Graves operator technique described in Acharya (2001). In this work, the spatial distribution of $\alpha_{33}(\mathbf{x})$ was given by

$$\alpha_{33}(\mathbf{x}) = \frac{b}{\pi r_0}\left(\frac{1}{r} - \frac{1}{r_0}\right) \quad \text{if } r \leqslant r_0$$
$$\alpha_{33}(\mathbf{x}) = 0 \quad \text{if } r > r_0 \tag{75}$$

with $r = \sqrt{x_1^2 + x_2^2}$.

Hence, the analytical expressions of T_{13} and T_{23} were directly derived from the incompatible part of elastic distortions (as in Eqs. (71) and (72)). They were found to be (Acharya, 2001)

$$T_{23} = \mu \frac{b}{2\pi}\left(\frac{x_1}{r^2}\right) \tag{76}$$

$$T_{13} = -\mu \frac{b}{2\pi}\left(\frac{x_2}{r^2}\right), \quad \text{if } r > r_0, \tag{77}$$

$$T_{23} = \mu \frac{b}{\pi r_0}\left(\frac{x_1}{r^2}\right)\left(r - \frac{r^2}{2r_0}\right) \tag{78}$$

$$T_{13} = -\mu \frac{b}{\pi r_0}\left(\frac{x_2}{r^2}\right)\left(r - \frac{r^2}{2r_0}\right), \quad \text{if } r \leqslant r_0 \tag{79}$$

The results for T_{13} and T_{23} are normalized by μ and shown in Fig. 3. The FFT results with 1024×1024 pixels and $\delta = 0.05b$ show very good agreement with the analytical formula given in Acharya (2001). Although the expression of $\alpha_{33}(\mathbf{x})$ is singular for $\mathbf{x} = 0$ (see Eq. (75)), the integral incompatibility equation (Eq. (17)) is verified with the FFT simulation, i.e.,

$$b = \int_S \alpha_{33}dS \tag{80}$$

Another assessment of the numerical spectral method is performed by regularizing the dislocation core with a Gaussian function defined by

$$\alpha_{33}(\mathbf{x}) = \frac{b}{2\pi\sigma^2}\exp\left(-\frac{r^2}{2\sigma^2}\right) \quad \text{if } r \leqslant r_0$$
$$\alpha_{33}(\mathbf{x}) = 0 \quad \text{if } r > r_0 \tag{81}$$

with $\sigma = 0.1r_0$.

Starting from Eq. (81), the FFT solutions obtained with 1024×1024 pixels and $\delta = 0.05b$ are compared to the classical analytical solutions for infinitely straight dislocations in linear elastic media (Hirth and Lothe, 1982), where the dislocation densities are represented by delta Dirac functions. These solutions correspond to Eqs. (76) and (77). Fig. 4 shows a very good agreement of the present FFT results with the analytical solutions, except at $\mathbf{x} = 0$ where classic solutions are singular. Furthermore, Eq. (80) is exactly verified in the case of a Gaussian regularization with $\sigma = 0.1r_0$ and the stress field inside and near the core region is very accurately predicted.

6.2.2. Comparisons of FFT with FEM results

In the following, the present FFT method is compared with finite element (FE) simulations solving the same Poisson-type equations (Eqs. (69) and (70)) with periodic boundary conditions. The FE method uses two-dimensional linear triangular continuous P1 finite elements and the GMRES solver (Gradient Minimal Residual) which allows to adopt large meshes with the free FEM code FreeFEM++ (Hecht, 2012).

Fig. 5 compares the profiles of T_{13} and T_{23} normalized by μ (contours) obtained by FFT (Fig. 5(a) and (c)) and FEM (Fig. 5(b) and (d)), in the case of the Gaussian dislocation distribution, with $\sigma = 0.1r_0$. For the same Gaussian regularization, the contours of ω_{31}^e and ω_{32}^e, obtained with Eqs. (73) and (74), and solved with FFT or FEM are compared in Fig. 6. Both elastic fields show very good agreement. It was also checked that the analytical solutions and contours obtained with Eqs. (76)–(79) (Acharya, 2001) give similar stress and elastic rotation contours.

To summarize these simulations, it is observed that both FFT and FEM solutions are very accurate methods to compute elastic fields of dislocations. However, the present FFT method with relatively large unit cell size is rather attractive in terms of computation time. Indeed, considering a single core 2.97 GHz Intel i7 (8Go, 1600 MHz DDR3), the CPU time needed with the FFT method is 6.3 s whereas it reaches ~20 min with the FE method using linear elements. It is expected that this gain in CPU time will be even more important for a three-dimensional problem (with an increase of the number of degrees of freedom) solving simultaneously both Poisson and Navier-type equations.

6.2.3. Single edge dislocation

A single infinitely straight edge dislocation is represented by a dislocation line lying along the $\mathbf{e}_3$ axis with Burgers vector $\mathbf{b} = b\mathbf{e}_1$ and unit line vector $\mathbf{t} = \mathbf{e}_3$. Thus, the dislocation density tensor contains only the $\alpha_{13}(\mathbf{x})$ component. Here, only a Gaussian distribution for the dislocation density is considered:
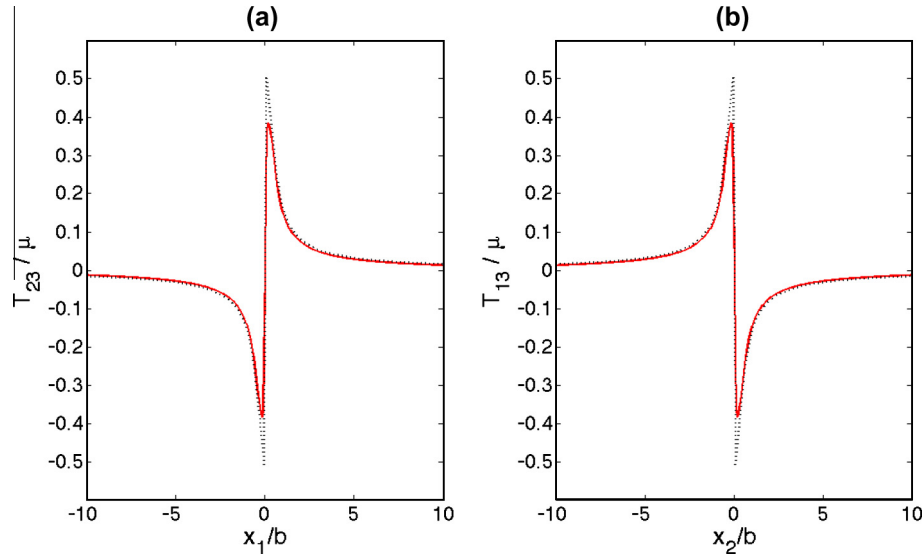
Fig. 3. Shear stress components T_{13} and T_{23} normalized by μ for a screw dislocation: FFT (solid lines) vs. analytical formula obtained with the Riemann-Graves operator technique (dashed lines) (Acharya, 2001).
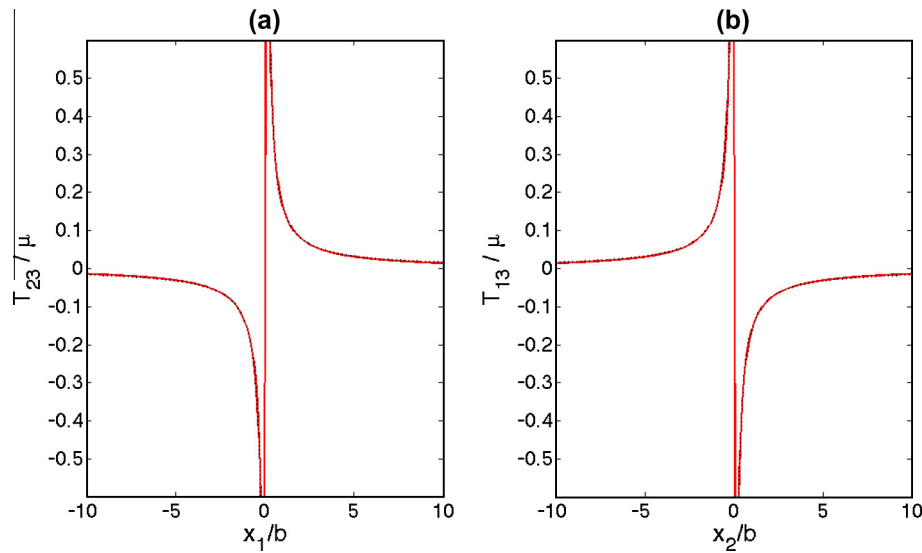

Fig. 4. Profiles of shear stress components T_{13} and T_{23} normalized by μ for a screw dislocation: FFT (solid lines) vs. analytical formula (dashed lines) (Hirth and Lothe, 1982).

$$\alpha_{13}(\boldsymbol{x}) = \frac{b}{2\pi\sigma^2} \exp\left(-\frac{r^2}{2\sigma^2}\right) \quad \text{if } r \leqslant r_0$$
$$\alpha_{13}(\boldsymbol{x}) = 0 \quad \text{if } r > r_0 \tag{82}$$

with $\sigma = 0.1 r_0$.

For an edge dislocation, the general Poisson-type equation (37) reduces to two independent equations

$$U_{11,11}^{e,\perp} + U_{11,22}^{e,\perp} = -\alpha_{13,2} \tag{83}$$

$$U_{12,11}^{e,\perp} + U_{12,11}^{e,\perp} = \alpha_{13,1} \tag{84}$$

After calculating the FFT of α_{13}, i.e. $\widehat{\alpha_{13}}$ using Eq. (57) together with Eq. (82), the non zero incompatible elastic distortion components $\widehat{U_{11}^{e,\perp}}$ and $\widehat{U_{12}^{e,\perp}}$ are first derived using Appendix A (Eqs. (A.4)–(A.6)).

Then, the Navier-type equation is solved using Appendix B to derive $\widehat{w_1}$ and $\widehat{w_2}$ (see Eqs. (B.1)–(B.7)). Finally, the four compatible parts of elastic distortions $\widehat{U_{11}^{e,\parallel}}, \widehat{U_{22}^{e,\parallel}}, \widehat{U_{12}^{e,\parallel}}$ and $\widehat{U_{21}^{e,\parallel}}$ are simply derived

from $\widehat{w_1}$ and $\widehat{w_2}$ using Eqs. (B.8)–(B.11). Inverse FFT (Eq. (58)) is used to compute $U_{11}^{e,\parallel}, U_{12}^{e,\parallel}, U_{22}^{e,\parallel}, U_{21}^{e,\parallel}, U_{12}^{e,\perp}$ and $U_{11}^{e,\perp}$ in the real spatial domain. The stress components $\widehat{T_{11}}, \widehat{T_{22}}, \widehat{T_{12}}$ are first derived from the isotropic elastic Hooke's law in the Fourier space (see Eqs. (53)–(56)). Stress self-equilibrium was verified in the Fourier space and the stress components were obtained in the real spatial domain by inverse FFT.

Profiles of stresses T_{11}, T_{22}, T_{12} (normalized by μ) obtained by FFT with 1024×1024 pixels (with $\delta = 0.05b$) for a Gaussian distribution of an infinitely straight edge dislocation ($\sigma = 0.1 r_0$) are compared with the analytical solutions of Hirth and Lothe (1982) in Fig. 7.

The results show that the present spectral method with a Gaussian dislocation density distribution leads to very accurate results compared to the analytical solution given in Hirth and Lothe (1982). In particular, a good correspondence is obtained between the tensile stresses T_{11}, T_{22}. Furthermore, the following integral form is exactly verified:
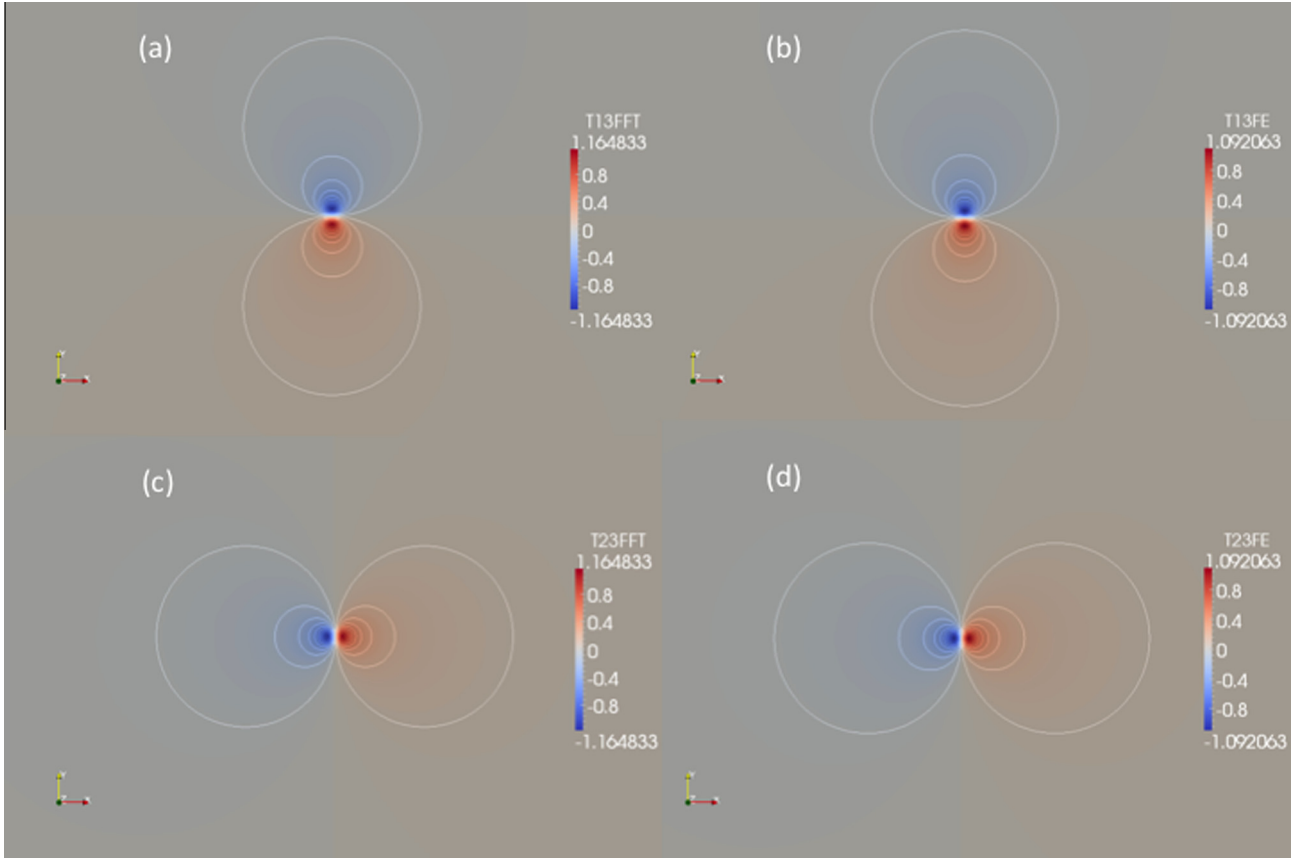
Fig. 5. Comparisons of the contours of shear stresses T_{13} (a,b) and T_{23} (c,d) (normalized by μ) for a Gaussian distribution of an infinitely straight screw dislocation ($\sigma = 0.1r_0$), obtained by FFT with 1024×1024 pixels (a,c), and, by FEM with 1024×1024 pixels (b,d), each pixel being composed of two triangular finite elements.

$$b = \int_S \alpha_{13} dS \tag{85}$$

The contours obtained for T_{11} (normal stress) and T_{12} (shear stress) normalized by μ (Fig. 8) typically represent edge dislocation normal and shear stress contours (Hirth and Lothe, 1982). Therefore, the present FFT-based method appears to be very well suited for the representation of single dislocations.

6.3. G-disclinations

6.3.1. Main equations

In the following applications, we consider straight g-disclinations such that the defect line lies along the $\mathbf{e}_3$ axis. Here, the defect is based on elastic distortion discontinuities described by non zero jumps $[\![U^e_{12}]\!]$ and $[\![U^e_{21}]\!]$. Thus, in this case, Eqs. (20) and (21) simplify into

$$\int_S \pi_{123} dS = \int_S \left(G^{e,\perp}_{122,1} - G^{e,\perp}_{121,2} \right) dS = [\![U^e_{12}]\!] \tag{86}$$

$$\int_S \pi_{213} dS = \int_S \left(G^{e,\perp}_{212,1} - G^{e,\perp}_{211,2} \right) dS = [\![U^e_{21}]\!] \tag{87}$$

Consequently, given $\pi_{123}(\mathbf{x})$ and $\pi_{213}(\mathbf{x})$, the incompatible elastic 2-distortions are solutions of the four following Poisson-type equations (see Eq. (30))

$$G^{e,\perp}_{122,11} + G^{e,\perp}_{122,22} = \pi_{123,1} \tag{88}$$

$$G^{e,\perp}_{121,11} + G^{e,\perp}_{121,22} = -\pi_{123,2} \tag{89}$$

$$G^{e,\perp}_{212,11} + G^{e,\perp}_{212,22} = \pi_{213,1} \tag{90}$$

$$G^{e,\perp}_{211,11} + G^{e,\perp}_{211,22} = -\pi_{213,2} \tag{91}$$

Once $G^{e,\perp}_{122}, G^{e,\perp}_{121}, G^{e,\perp}_{212}$ and $G^{e,\perp}_{211}$ are obtained, four other Poisson-type equations are needed to find in turn the incompatible elastic 1-distortions $U^{e,\perp}_{11}, U^{e,\perp}_{22}, U^{e,\perp}_{12}$ and $U^{e,\perp}_{21}$ using Eq. (37) (without prescribing dislocation densities)

$$U^{e,\perp}_{12,11} + U^{e,\perp}_{12,22} = -G^{e,\perp}_{121,1} \tag{92}$$

$$U^{e,\perp}_{11,11} + U^{e,\perp}_{11,22} = G^{e,\perp}_{121,2} \tag{93}$$

$$U^{e,\perp}_{21,11} + U^{e,\perp}_{21,22} = -G^{e,\perp}_{212,2} \tag{94}$$

$$U^{e,\perp}_{22,11} + U^{e,\perp}_{22,22} = G^{e,\perp}_{212,1} \tag{95}$$

All the previous equations will be solved successively in the Fourier space in the cases of a straight wedge disclination, a wedge disclination dipole, a single twin tip and a "twinning g-disclination" considered as a twin tip dipole. Then, the Navier-type equation is solved in the Fourier space for the compatible elastic distortions (see Section 4.2) to finally derive the stress components, as done in Section 4.3.

6.3.2. Straight wedge disclination and dipole

First, the case of pure straight wedge disclination (commonly used to describe tilt grain boundaries) is considered. This corresponds to an elastic distortion discontinuity in the negative half-plane ($x_1 = 0, x_2 \leqslant 0$). The only non zero discontinuities are $[\![U^e_{12}]\!] = [\![\omega^e_{12}]\!] = -[\![\Omega^e_3]\!]$ and $[\![U^e_{21}]\!] = [\![\omega^e_{21}]\!] = +[\![\Omega^e_3]\!]$, where $[\![\Omega^e_3]\!] = \Omega^e_{3+} - \Omega^e_{3-}$ is the elastic rotation jump along the $\mathbf{e}_3$ axis (the domains (+) and (−) respectively correspond to $x_1 > 0$ and $x_1 < 0$). This g-disclination is equivalent to a pure disclination with the Frank vector component along the $\mathbf{e}_3$ axis (Romanov and Vladimirov, 1992) with $[\![\Omega^e_3]\!] = \omega$. Thus, the discontinuity in the elastic distortion is such that
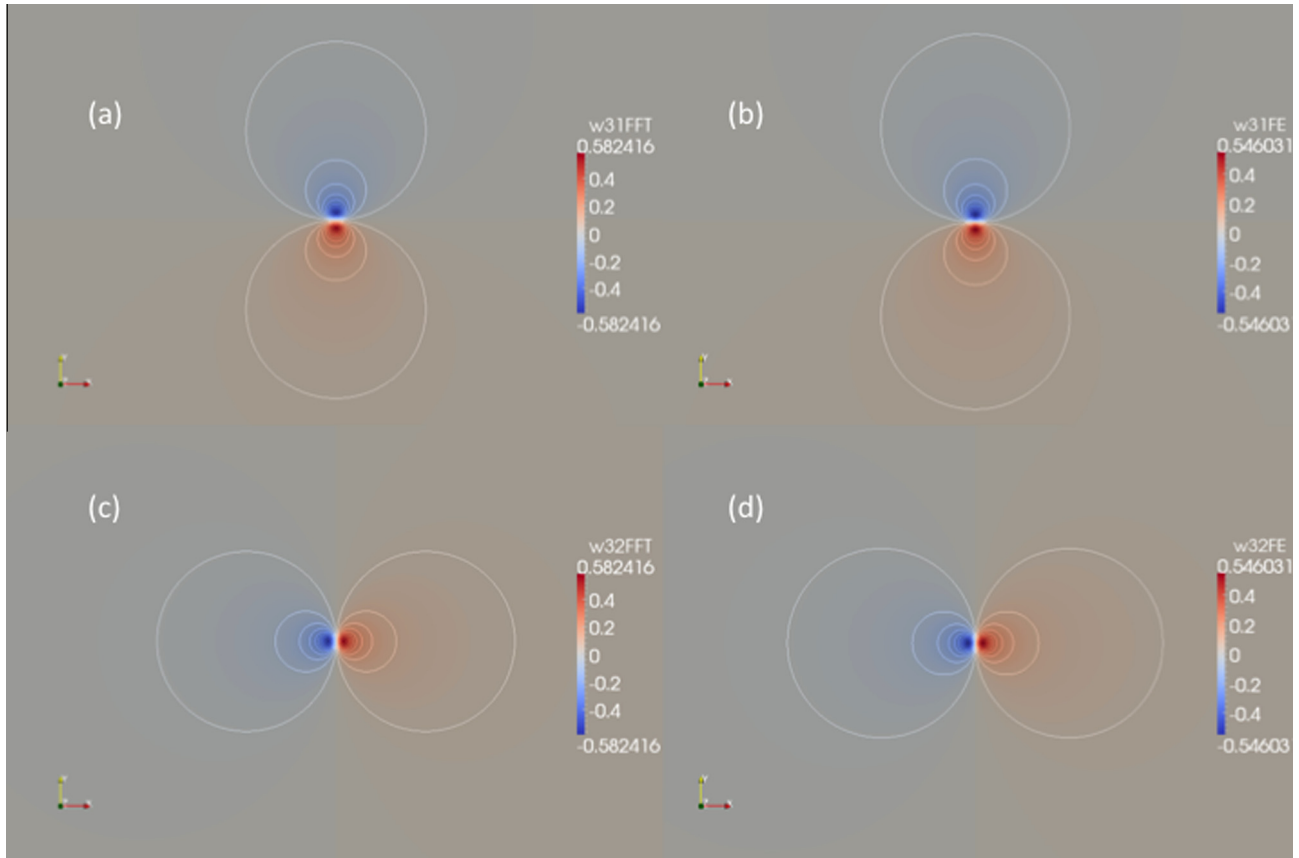
Fig. 6. Comparisons of the contours of elastic rotations ω_{31}^e (a,b) and ω_{32}^e (c,d) (in radians) for a Gaussian distribution of an infinitely straight screw dislocation ($\sigma = 0.1r_0$), obtained by FFT with 1024×1024 pixels (a,c), and, by FEM with 1024×1024 pixels (b,d), each pixel being composed of two triangular finite elements.
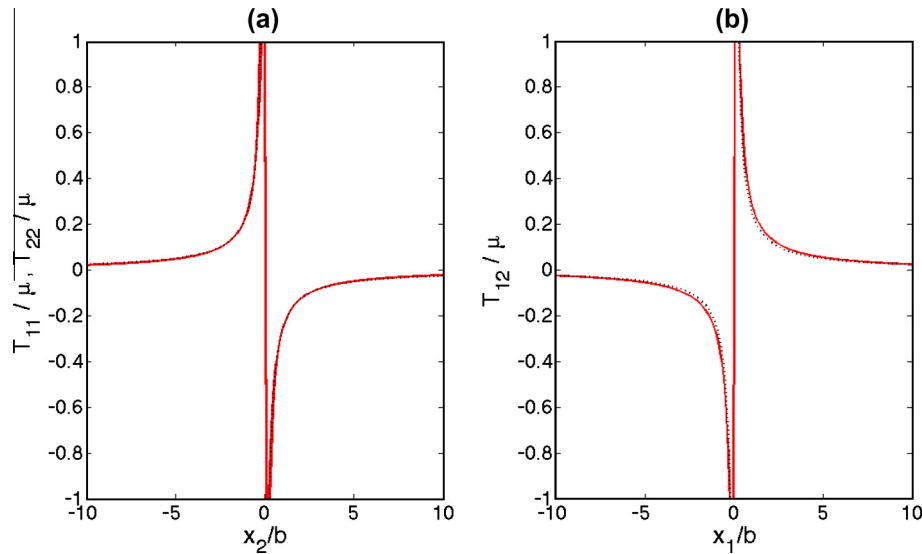

Fig. 7. Profiles of stress components: (a) T_{11}, T_{22} and (b) T_{12} normalized by μ for a straight edge dislocation: FFT (solid lines) vs. analytical formulas (dashed lines) (Hirth and Lothe, 1982).

$$\llbracket \Omega_3^e \rrbracket = \int_S \pi_{213} dS \qquad (96)$$

where $\pi_{213} = -\pi_{123}$. Thus, only two Poisson-type equations containing π_{213} are considered and solved in the Fourier space using Appendix A. For the simulations, the g-disclination density follows a Gaussian distribution:

$$\pi_{213}(\boldsymbol{x}) = \frac{\llbracket \Omega_3^e \rrbracket}{2\pi\sigma^2} \exp\left(-\frac{r^2}{2\sigma^2}\right) \quad \text{if } r \leqslant r_0$$

$$\pi_{213}(\boldsymbol{x}) = 0 \quad \text{if } r > r_0 \qquad (97)$$

with $r = \sqrt{x_1^2 + x_2^2}$ and $\sigma = 0.1r_0$. Then, the non zero (incompatible) elastic curvature components (equivalent to incompatible elastic 2-distortions) are obtained as
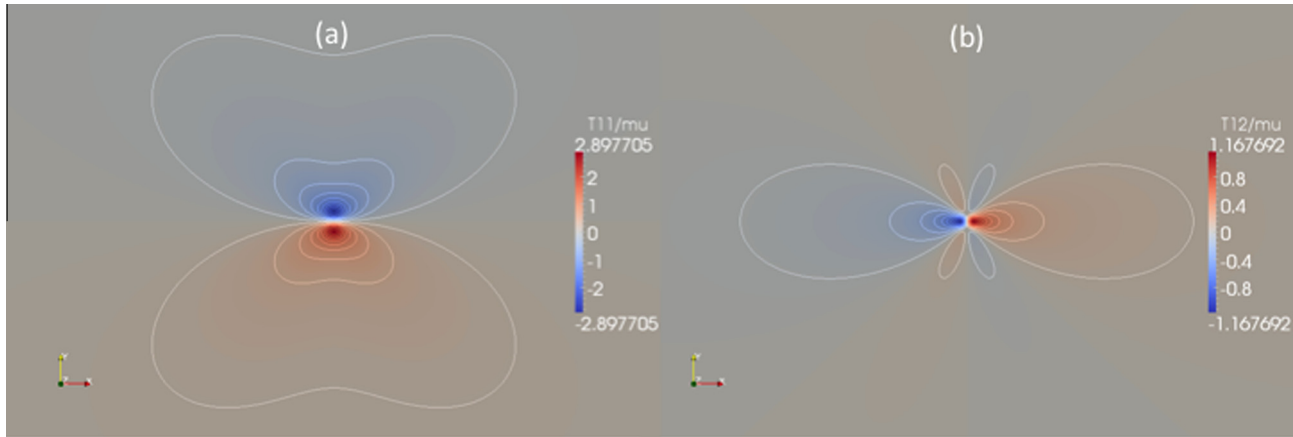
Fig. 8. Stress contours: (a) T_{11} and (b) T_{12} normalized by μ for a straight edge dislocation obtained by FFT with 1024×1024 pixels.

$$\kappa_{31}^e = -G_{121}^{e,\perp} \tag{98}$$
$$\kappa_{32}^e = -G_{122}^{e,\perp} \tag{99}$$

The elastic curvatures κ_{32}^e and κ_{31}^e are reported on Fig. 9. They are obtained from Eqs. (A.7)–(A.9) (see Appendix A) by inverse FFT on a 2D grid with 1024×1024 pixels, $\delta = 0.1b$ and using $[\![\Omega_3^e]\!] = 5/6$ rad. The results show that the respective variations of κ_{32}^e and κ_{31}^e along x_1 and x_2 match exactly the analytical solutions of deWit (1973)

$$\kappa_{31}^e = -\frac{[\![\Omega_3^e]\!]}{2\pi} \frac{x_2}{r^2} \tag{100}$$
$$\kappa_{32}^e = \frac{[\![\Omega_3^e]\!]}{2\pi} \frac{x_1}{r^2} \tag{101}$$

A second application is the case of a wedge disclination dipole as described in Fig. 10. The positive (resp. negative) pole is distributed by using the same Gaussian distribution as in Eq. (97) at location $(x_1 = 0, x_2 = +a)$ (resp. $(x_1 = 0, x_2 = -a)$) with disclination strength $[\![\Omega_3^e]\!]$ (resp. $-[\![\Omega_3^e]\!]$).

In order to get stress fields similar to that of an equivalent straight edge dislocation, the semi-length of the dipole is set to $a = b/(2[\![\Omega_3^e]\!])$ (see e.g. Romanov and Vladimirov, 1992) with $[\![\Omega_3^e]\!] = 5/6$ rad. For the FFT simulations, the stress components
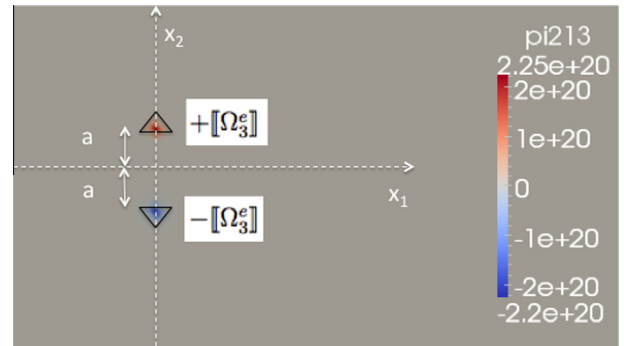

Fig. 10. Spatial distribution of G-disclination dipole density in $rad.m^{-2}$ (straight wedge disclination dipole) with associated positive and negative rotation jumps: $+[\![\Omega_3^e]\!]$ and $-[\![\Omega_3^e]\!]$.

are obtained by inverse FFT on a 2D grid (2048×2048 pixels, $\delta = 0.1b$) after successively computing in the discrete Fourier space the (incompatible) elastic curvatures, the incompatible elastic 1-distortions (see Appendix A, Eqs. (A.7)–(A.14)), the compatible elastic distortions (see Appendix B, Eqs. (B.1)–(B.11)) and the stresses using the Hooke's law. Stress self-equilibrium was verified in the Fourier space.
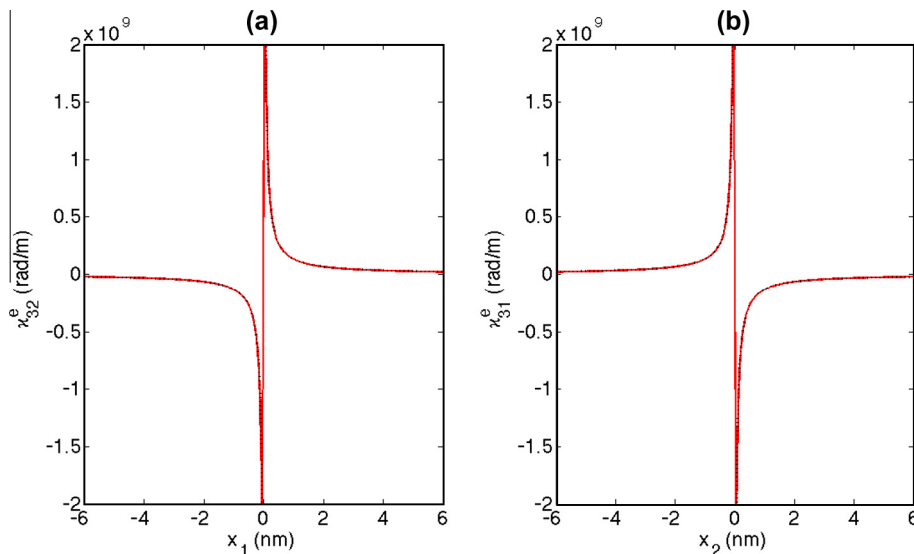

Fig. 9. Profiles of (incompatible) elastic curvatures for a straight wedge disclination: (a) κ_{32}^e, (b) κ_{31}^e: FFT (solid lines) vs. analytical formula (dashed lines) (deWit, 1973).
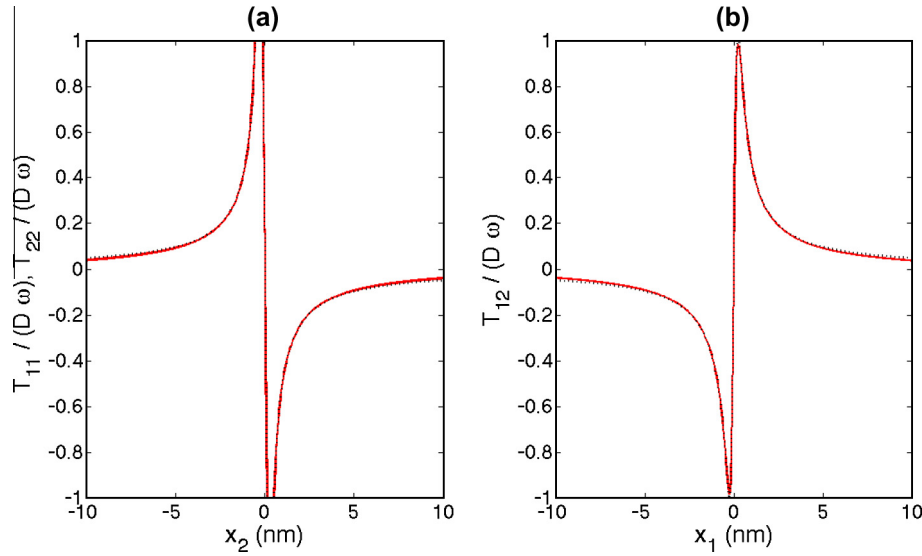
Fig. 11. Profiles of stress components: (a) T_{11}, T_{22}, (b) T_{12}, for a straight wedge disclination dipole (see Fig. 10) obtained by FFT and normalized by $D\omega$ where $\omega = [\![\Omega_3^e]\!]$ and $D = \mu/(2\pi(1-\nu))$ (solid lines). Comparisons with the analytical solutions given by deWit (1973); Romanov and Vladimirov, 1992 (dashed lines).

Fig. 11 displays the stress components T_{11}, T_{22}, T_{12} obtained by FFT and normalized by $D\omega$ where $\omega = [\![\Omega_3^e]\!]$ and $D = \mu/(2\pi(1-\nu))$. Excellent agreement is found with the analytical stress components given by deWit (1973) and Romanov and Vladimirov (1992) for wedge disclination dipoles. Furthermore, the present FFT results also confirm that the stress contours reported on Fig. 12 are similar to those of an edge dislocation (see Fig. 8).

6.3.3. Single twin tip and twinning g-disclination

Finally, pure g-disclinations describing first a twin-tip and, second, a twin-tip dipole are considered (Fig. 13).

First, the case of a single twin tip (Fig. 13(a)) corresponds to an elastic distortion discontinuity in the positive half-plane $(x_1 \geqslant 0, x_2 = 0)$. The only non zero discontinuities are $[\![U_{12}^e]\!] = [\![\varepsilon_{12}^e]\!]$ and $[\![U_{21}^e]\!] = [\![\varepsilon_{21}^e]\!] = [\![\varepsilon_{12}^e]\!]$, where $[\![\varepsilon_{12}^e]\!] = \varepsilon_{12+}^e - \varepsilon_{12-}^e = \frac{1}{2}s$ is the elastic shear strain discontinuity along the positive half-plane $(x_1 \geqslant 0, x_2 = 0)$ (the domains (+) and (−) correspond to $x_2 > 0$ and $x_2 < 0$, respectively). This half-plane can be interpreted as the twin boundary terminating along the g-disclination line between two crystals: the twin and the parent domains are such that the twin domain encounters a twin shear s depending on crystal symmetry. Here, a twinning shear s of $\frac{1}{\sqrt{2}}$ is considered for fcc
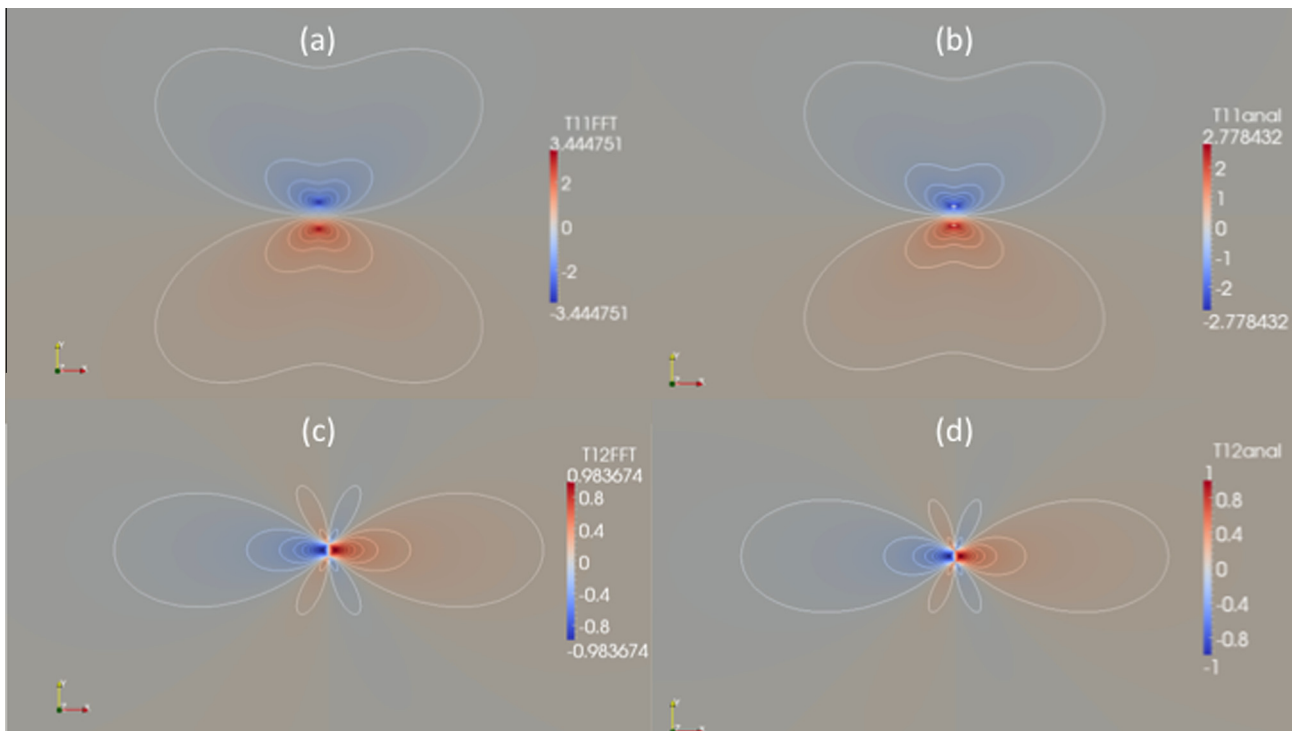

Fig. 12. Stress contours for T_{11} (top) and T_{12} (bottom) for a straight wedge disclination dipole (see Fig. 10) obtained by FFT (a,c) and normalized by $D\omega$ where $\omega = [\![\Omega_3^e]\!]$ and $D = \mu/(2\pi(1-\nu))$. Comparisons with the analytical solutions given by deWit (1973) and Romanov and Vladimirov (1992) (b,d).
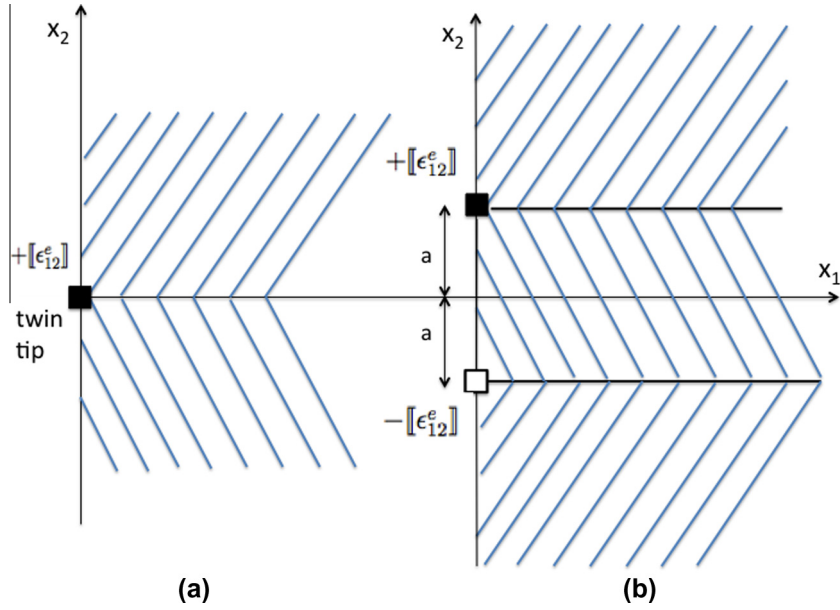
Fig. 13. Schematic view of (a) single twin tip, and, (b) twin tip dipole forming a semi-infinite twin of thickness 2a.

metals like Al (Christian and Mahajan, 1995). Thus, the discontinuity in the elastic shear strain is such that

$$[\![\varepsilon_{12}^e]\!] = \int_S \pi_{123} dS \tag{102}$$

where $\pi_{123} = \pi_{213}$. Thus, only two Poisson-type equations containing π_{123} are considered and solved in the Fourier space using Appendix A (Eqs. (A.15)–(A.17)).

For the simulations, the g-disclination density follows a Gaussian distribution:

$$\pi_{123}(\boldsymbol{x}) = \frac{[\![\varepsilon_{12}^e]\!]}{2\pi\sigma^2} \exp\left(-\frac{r^2}{2\sigma^2}\right) \quad \text{if } r \leqslant r_0$$

$$\pi_{123}(\boldsymbol{x}) = 0 \quad \text{if } r > r_0 \tag{103}$$

with $\sigma = 0.1 r_0$.

Then, the two independent non zero incompatible elastic 2-distortion components useful to compute the incompatible elastic 1-distortions are

$$G_{121}^{e,\perp} = G_{211}^{e,\perp} \tag{104}$$

$$G_{122}^{e,\perp} = G_{212}^{e,\perp} \tag{105}$$

They are numerically computed onto a 2D grid with 1024×1024 pixels and with $\delta = 0.1b$. The FFT results are reported on Fig. 14. They show excellent agreement with the analytical expressions derived from the Riemann-Graves operator technique (Fressengeas and Acharya, 2014):

$$G_{121}^{e,\perp} = -\frac{[\![\varepsilon_{12}^e]\!]}{2\pi} \frac{x_2}{r^2} \tag{106}$$

$$G_{122}^{e,\perp} = \frac{[\![\varepsilon_{12}^e]\!]}{2\pi} \frac{x_1}{r^2} \tag{107}$$
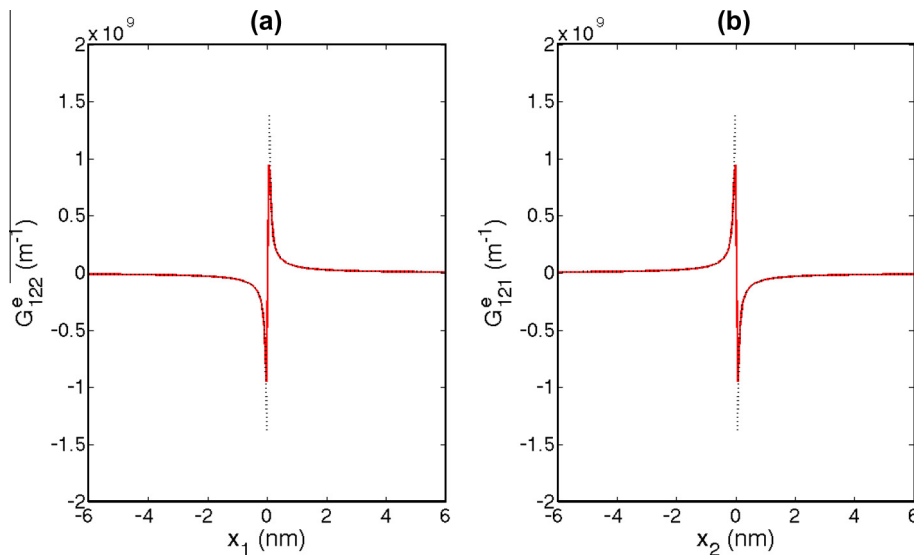

Fig. 14. Profiles of incompatible elastic 2-distortion components: (a) $G_{122}^{e,\perp}$, (b) $G_{121}^{e,\perp}$ obtained by FFT (solid lines) and comparison with analytical expressions given by Fressengeas and Acharya (2014) (dashed lines).
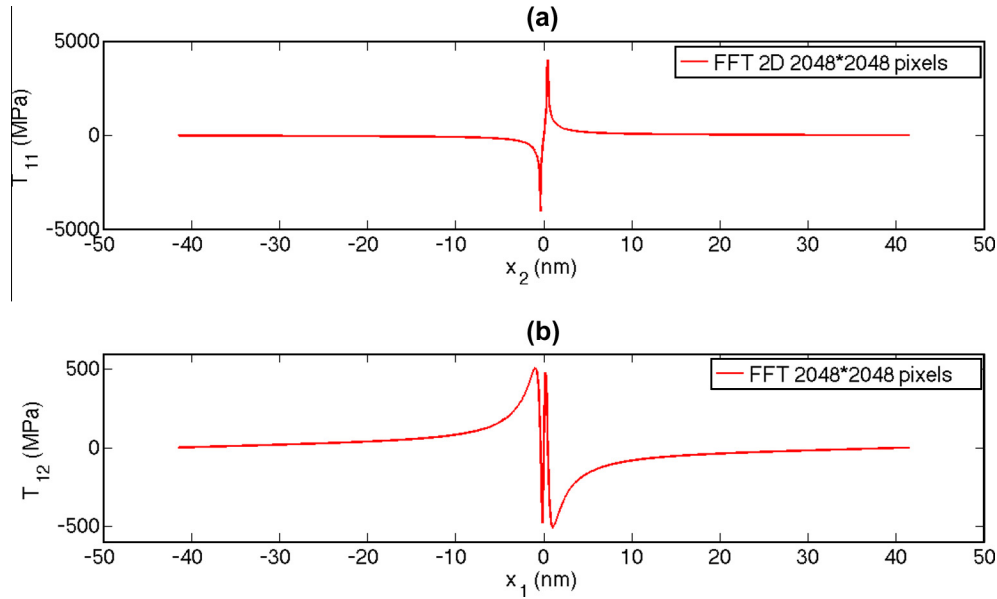
Fig. 15. Profiles of normal stress T_{11} (in MPa) as a function of x_2 ($x_1 = 0$), and shear stress T_{12} (in MPa) as a function of x_1 ($x_2 = 0$), induced by a dipole of twin tip of opposite signs for a twin of thickness $2a = 2b$.

Second, the stress field of a twinning g-disclination (semi-infinite twin of thickness $2a$ defined for $x_1 \geqslant 0$) corresponding to a twin tip dipole is investigated (Fig. 13(b)). The positive (resp. negative) pole is distributed by using the same Gaussian distribution as in Eq. (103) at location ($x_1 = 0, x_2 = +a$) (resp. ($x_1 = 0, x_2 = -a$)) with g-disclination strength $[\![\varepsilon_{12}^e]\!]$ (resp. $-[\![\varepsilon_{12}^e]\!]$).

The incompatible elastic 1-distortions of the semi-infinite twin are computed in the discrete Fourier space using Eqs. (A.18)–(A.22) and the stresses are obtained by inverse FFT after using the equations of Appendix B (Eqs. (B.1)–(B.11)). Considering a unit cell discretized with 2048×2048 pixels (with a pixel size of $0.1b$), a twin shear $s = \sqrt{2}/2$, the normal stress T_{11} and the shear stress T_{12} are reported in MPa on Fig. 15. It is seen that these stresses are very large in magnitude close to twin tips. The influence of twin thickness on the normal and shear stresses is investigated in Fig. 16.

When the twin is very thin like $2b$ (Fig. 15), it is found that the stress variation is not as spread out across the dipole as when the twin thickness is $10b$ (Fig. 16).

7. Discussion

When restricting the dislocation density of a single dislocation to one pixel in the center of a unit cell, strong numerical Gibbs oscillations have been very recently reported in Brenner et al. (2014). Similarly to the classic work of Moulinec and Suquet (1998), their method to compute the stress field of dislocations is based on a discrete approximation of the continuous Fourier transform for $\widetilde{\mathbf{T}}(\xi)$ given by Eq. (54), which is different from the present FFT method based on a 9-pixel approximation with FFT differentiation rules given in Section 5.2.
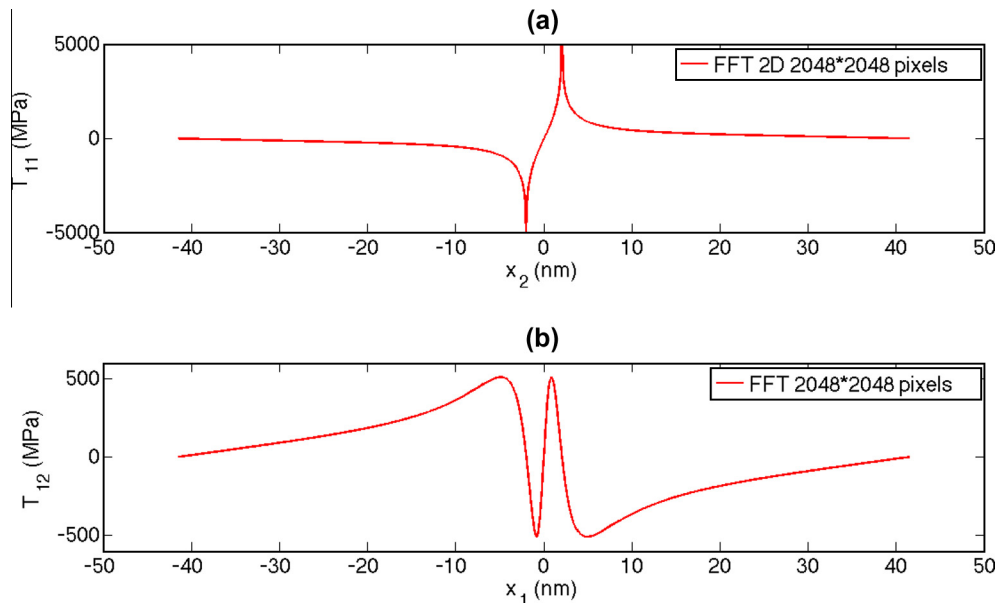

Fig. 16. Profiles of normal stress T_{11} (in MPa) as a function of x_2 ($x_1 = 0$), and shear stress T_{12} (in MPa) as a function of x_1 ($x_2 = 0$), induced by a dipole of twin tip of opposite signs for a twin of thickness $2a = 10b$.
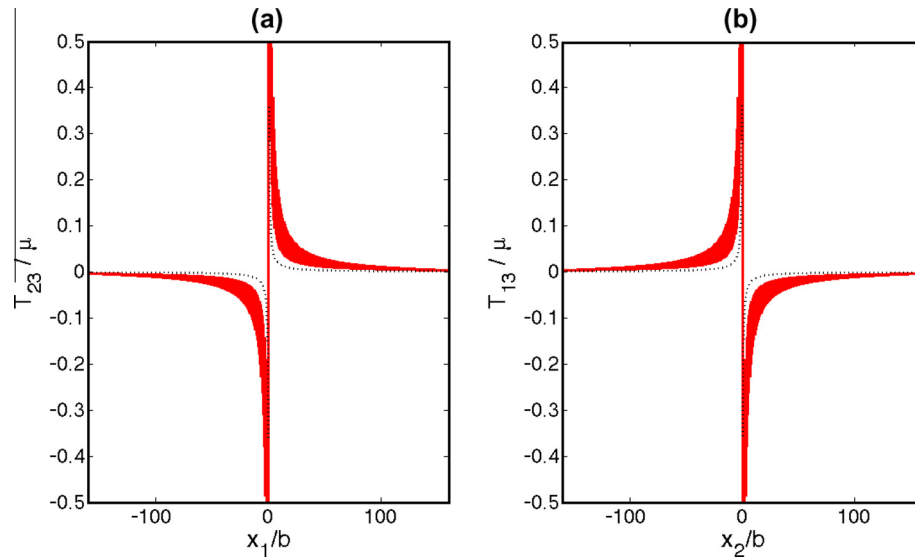
Fig. 17. Numerical Gibbs oscillations observed on T_{13} and T_{23} obtained with the classical FFT approximation for a single screw dislocation with dislocation density α_{33} located on a single pixel at the center of the unit cell. The analytical solutions are represented by dashed lines.

Considering a unit cell dimension of $450b \times 450b$ discretized with 1024×1024 pixels and using the same material parameters as those introduced in 6.1, their results are reproduced in Figs. 17 by using a discrete approximation of continuous Fourier transforms given by Eq. (53) and Eq. (44) (without considering g-disclination densities and incompatible 2-distortion) for a single straight screw dislocation. For the simulations, a dislocation density $\alpha_{33} = b/\delta^2$ is distributed in a single pixel in the center of the unit cell, verifying Eq. (80). Furthermore, a coarser pixel size is used as compared to previous simulations in Section 6. Gibbs oscillations are observed in comparison with the exact analytical solutions for T_{13} (resp. T_{23}) given by Hirth and Lothe (1982).

The application of the present FFT method for the same dislocation density $\alpha_{33} = b/\delta^2$ distributed on a single pixel (also verifying Eq. (80)) does not lead to Gibbs oscillations and gives accurate solutions as compared to analytical ones, see Fig. 18. Thus, it seems more efficient than the classical approximation since there is no need to spread the dislocation density on several pixels in the dislocation core to avoid Gibbs oscillations.

In the core spreading treatment reported by Brenner et al. (2014), a triangular distribution of the screw dislocation density over a surface of 3×3 pixels is adopted to avoid Gibbs oscillations and to retrieve the shear stress field, instead of a dislocation density concentrated on a single pixel. The triangulation is set up with different dislocation density weights assigned to 9 pixels within the dislocation core to ensure the integral incompatibility form for a screw dislocation (Eq. (80)) and to match the analytical solution without any oscillation.

In the present DFT-based methodology, we did not observe any Gibbs oscillation by using the differentiation rules based on intrinsic discrete Fourier transforms, not only for regularized Gaussian distributions of defect cores (see Section 6), but also with a uniform defect density restricted to a single pixel (this section). Hence, the present DFT approach, based on a 9-pixel centered finite difference for the calculation of spatial derivatives, is not equivalent to a spreading of core defect densities. Such a spreading is actually not needed and core defect densities concentrated on a single pixel can be conveniently solved, without any Gibbs oscillation. It is
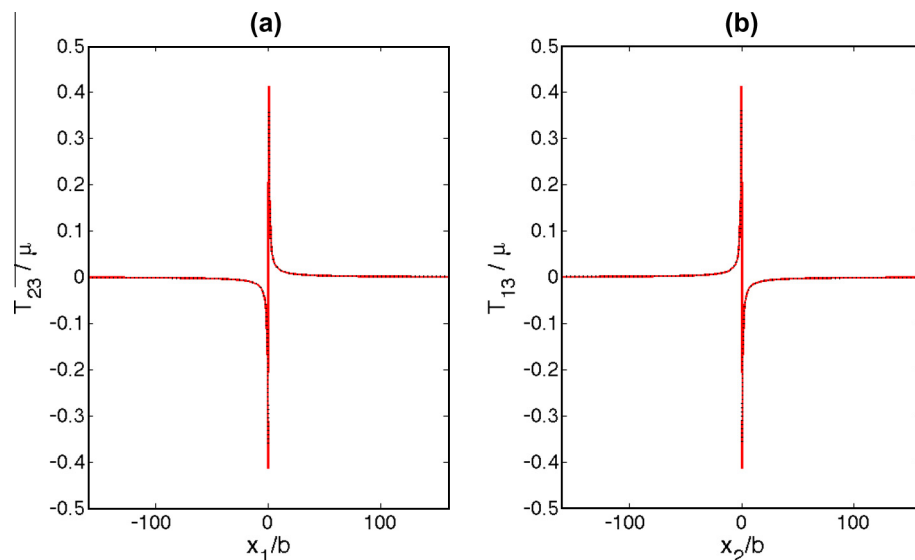

Fig. 18. Solutions without Gibbs oscillations for T_{13} and T_{23} obtained with the present FFT formulation for a single screw dislocation with dislocation density α_{33} located on a single pixel at the center of the unit cell. The analytical solutions are represented by dashed lines.

indeed observed that the present approach is consistent with the pixel grid through the differentiation rules (Eqs. (64)–(68)) and leads to very accurate results when the defect core region is set up to the pixel size. Similar arguments but in another context (FFT-based approach for the electric response of heterogeneous media) were recently reported in Willot et al. (2014). In their work, a discrete FT Green operator based on forward difference differentiation rules (more adapted to conductivity problems), was developed in order to improve the accuracy of local field predictions with FFT, as compared to the classic continuous FT Green operator, especially when strong spatial gradients of the solution exist near discontinuity interfaces.

8. Conclusions

A new spectral approach for periodic media is developed to solve the elasto-static equations of field dislocation and g-disclination mechanics. Such approach may be useful to simulate large ensembles of dislocations or g-disclinations in crystalline solids.

Various original results are obtained such as the solutions of Poisson-type equations in the Fourier space for a medium containing both dislocation and g-disclination densities. These solutions capture the incompatible part of elastic fields induced by the defects in the Fourier space. The compatible part of elastic fields needed to retrieve the Cauchy stress field is obtained from the solution of a Navier-type equation in the Fourier space.

The present "intrinsic" discrete Fourier transform method uses the FFT algorithm and has been adapted to 2D periodic unit cells containing infinitely straight defect lines in a isotropic and homogeneous elasticity framework. The discrete Fourier transform method is based on differentiation rules allowing exact calculations of FFT coefficients for periodic media.

The accuracy of the method was verified by studying different particular cases like screw, edge dislocations, wedge disclinations and twin tips. The FFT solutions were compared to available analytical solutions for dislocations and disclinations. The FFT simulations were also successfully compared to FEM results for a screw dislocation with similar boundary conditions. These simulations have shown the efficiency of the present FFT numerical method in term of CPU time as compared to finite elements. The present FFT method also avoids spurious Gibbs oscillations which are commonly observed in classical FFT approximations, especially when dislocation density is located on a single pixel. Therefore, it is well adapted to studies of crystal defect cores, where strong spatial field variations are expected.

Further studies will be dedicated to three-dimensional applications, such as polycrystals. Plasticity caused by the motion of defects will also be considered and will require an extension of the present spectral approach to dislocation/g-disclination transport.

Acknowledgements

Appendix A. FFT solutions of Poisson-type equations for single straight defects

A.1. Dislocations: case of straight screw and edge dislocations

In the case of an infinite straight screw dislocation, the FFT of α_{33} denoted $\widehat{\alpha_{33}}$ is first calculated using Eq. (57). Second, the solutions of Poisson's equations for $\widehat{U_{32}^{e,\perp}}$ and $\widehat{U_{31}^{e,\perp}}$ are obtained in the

Fourier space using the discrete FFT algorithm as follows $\forall(k,l) \neq (1,1)$

$$\widehat{U_{32}^{e,\perp}}(k,l) = \mathrm{i}\frac{\delta}{2}\frac{\sin\left(\frac{2\pi(k-1)}{N_1}\right)}{\cos\left(2\pi\left(\frac{(k-1)}{N_1}\right)\right) + \cos\left(2\pi\left(\frac{(l-1)}{N_2}\right)\right) - 2}\widehat{\alpha_{33}}(k,l) \quad (A.1)$$

$$\widehat{U_{31}^{e,\perp}}(k,l) = -\mathrm{i}\frac{\delta}{2}\frac{\sin\left(\frac{2\pi(l-1)}{N_2}\right)}{\cos\left(2\pi\left(\frac{(k-1)}{N_1}\right)\right) + \cos\left(2\pi\left(\frac{(l-1)}{N_2}\right)\right) - 2}\widehat{\alpha_{33}}(k,l) \quad (A.2)$$

and,

$$\widehat{U_{32}^{e,\perp}}(1,1) = \widehat{U_{31}^{e,\perp}}(1,1) = 0 \quad (A.3)$$

In the case of an infinite straight edge dislocation, the FFT of α_{13} denoted $\widehat{\alpha_{13}}$ is first calculated using Eq. (57). Then, the non zero incompatible elastic distortion components are obtained in the discretized Fourier space as follows $\forall(k,l) \neq (1,1)$

$$\widehat{U_{11}^{e,\perp}}(k,l) = -\mathrm{i}\frac{\delta}{2}\frac{\sin\left(\frac{2\pi(l-1)}{N_2}\right)}{\cos\left(2\pi\left(\frac{(k-1)}{N_1}\right)\right) + \cos\left(2\pi\left(\frac{(l-1)}{N_2}\right)\right) - 2}\widehat{\alpha_{13}}(k,l) \quad (A.4)$$

$$\widehat{U_{12}^{e,\perp}}(k,l) = \mathrm{i}\frac{\delta}{2}\frac{\sin\left(\frac{2\pi(k-1)}{N_1}\right)}{\cos\left(2\pi\left(\frac{(k-1)}{N_1}\right)\right) + \cos\left(2\pi\left(\frac{(l-1)}{N_2}\right)\right) - 2}\widehat{\alpha_{13}}(k,l) \quad (A.5)$$

and,

$$\widehat{U_{11}^{e,\perp}}(1,1) = \widehat{U_{12}^{e,\perp}}(1,1) = 0 \quad (A.6)$$

A.2. G-disclinations: case of straight wedge disclination

In the case of an infinite straight wedge disclination, which is a special case of g-disclination, the FFT of π_{213} denoted $\widehat{\pi_{213}}$ is first calculated using Eq. (57). Then, the non zero and non redundant incompatible 2-distortions are given by two elastic curvature components obtained in the discretized Fourier space as follows $\forall(k,l) \neq (1,1)$

$$\widehat{\kappa_{31}^{e}}(k,l) = -\mathrm{i}\frac{\delta}{2}\frac{\sin\left(\frac{2\pi(l-1)}{N_2}\right)}{\cos\left(2\pi\left(\frac{(k-1)}{N_1}\right)\right) + \cos\left(2\pi\left(\frac{(l-1)}{N_2}\right)\right) - 2}\widehat{\pi_{213}}(k,l) \quad (A.7)$$

$$\widehat{\kappa_{32}^{e}}(k,l) = \mathrm{i}\frac{\delta}{2}\frac{\sin\left(\frac{2\pi(k-1)}{N_1}\right)}{\cos\left(2\pi\left(\frac{(k-1)}{N_1}\right)\right) + \cos\left(2\pi\left(\frac{(l-1)}{N_2}\right)\right) - 2}\widehat{\pi_{213}}(k,l) \quad (A.8)$$

and,

$$\widehat{\kappa_{31}^{e}}(1,1) = \widehat{\kappa_{32}^{e}}(1,1) = 0 \quad (A.9)$$

Once these elastic curvatures are calculated, the non zero incompatible elastic 1-distortion components are obtained in the discretized Fourier space as follows $\forall(k,l) \neq (1,1)$

$$\widehat{U_{11}^{e,\perp}}(k,l) = -\mathrm{i}\frac{\delta}{2}\frac{\sin\left(\frac{2\pi(l-1)}{N_2}\right)}{\cos\left(2\pi\left(\frac{(k-1)}{N_1}\right)\right) + \cos\left(2\pi\left(\frac{(l-1)}{N_2}\right)\right) - 2}\widehat{\kappa_{31}^{e}}(k,l) \quad (A.10)$$

$$\widehat{U_{22}^{e,\perp}}(k,l) = \mathrm{i}\frac{\delta}{2}\frac{\sin\left(\frac{2\pi(k-1)}{N_1}\right)}{\cos\left(2\pi\left(\frac{(k-1)}{N_1}\right)\right) + \cos\left(2\pi\left(\frac{(l-1)}{N_2}\right)\right) - 2}\widehat{\kappa_{32}^{e}}(k,l) \quad (A.11)$$

$$\widehat{U_{12}^{e,\perp}}(k,l) = \mathrm{i}\frac{\delta}{2}\frac{\sin\left(\frac{2\pi(k-1)}{N_1}\right)}{\cos\left(2\pi\left(\frac{(k-1)}{N_1}\right)\right) + \cos\left(2\pi\left(\frac{(l-1)}{N_2}\right)\right) - 2}\widehat{\kappa_{31}^{e}}(k,l) \quad (A.12)$$

$$\widehat{U_{21}^{e,\perp}}(k,l) = -\mathrm{i}\frac{\delta}{2}\frac{\sin\left(\frac{2\pi(l-1)}{N_2}\right)}{\cos\left(2\pi\left(\frac{(k-1)}{N_1}\right)\right) + \cos\left(2\pi\left(\frac{(l-1)}{N_2}\right)\right) - 2}\widehat{\kappa_{32}^{e}}(k,l) \quad (A.13)$$

and,

$$\widehat{U_{11}^{e,\perp}}(1,1) = \widehat{U_{11}^{e,\perp}}(1,1) = \widehat{U_{12}^{e,\perp}}(1,1) = \widehat{U_{21}^{e,\perp}}(1,1) = 0 \qquad (A.14)$$

A.3. G-disclinations: case of twin tip

In the case of an infinite twin tip, the FFT of π_{123} denoted $\widehat{\pi_{123}}$ is first calculated using Eq. (57). Then, the non zero and non redundant incompatible 2-distortions are given in the discretized Fourier space as follows $\forall (k,l) \neq (1,1)$

$$\widehat{G_{121}^{e,\perp}}(k,l) = -\mathrm{i}\frac{\delta}{2}\frac{\sin\left(\frac{2\pi(l-1)}{N_2}\right)}{\cos\left(2\pi\left(\frac{(k-1)}{N_1}\right)\right)+\cos\left(2\pi\left(\frac{(l-1)}{N_2}\right)\right)-2}\widehat{\pi_{123}}(k,l) \quad (A.15)$$

$$\widehat{G_{122}^{e,\perp}}(k,l) = \mathrm{i}\frac{\delta}{2}\frac{\sin\left(\frac{2\pi(k-1)}{N_1}\right)}{\cos\left(2\pi\left(\frac{(k-1)}{N_1}\right)\right)+\cos\left(2\pi\left(\frac{(l-1)}{N_2}\right)\right)-2}\widehat{\pi_{123}}(k,l) \quad (A.16)$$

and,

$$\widehat{G_{121}^{e,\perp}}(1,1) = \widehat{G_{122}^{e,\perp}}(1,1) = 0 \qquad (A.17)$$

Once these incompatible elastic 2-distortions are calculated, the non zero incompatible elastic 1-distortion components are obtained in the discretized Fourier space as follows $\forall (k,l) \neq (1,1)$

$$\widehat{U_{11}^{e,\perp}}(k,l) = \mathrm{i}\frac{\delta}{2}\frac{\sin\left(\frac{2\pi(l-1)}{N_2}\right)}{\cos\left(2\pi\left(\frac{(k-1)}{N_1}\right)\right)+\cos\left(2\pi\left(\frac{(l-1)}{N_2}\right)\right)-2}\widehat{G_{121}^{e,\perp}}(k,l) \quad (A.18)$$

$$\widehat{U_{22}^{e,\perp}}(k,l) = \mathrm{i}\frac{\delta}{2}\frac{\sin\left(\frac{2\pi(k-1)}{N_1}\right)}{\cos\left(2\pi\left(\frac{(k-1)}{N_1}\right)\right)+\cos\left(2\pi\left(\frac{(l-1)}{N_2}\right)\right)-2}\widehat{G_{122}^{e,\perp}}(k,l) \quad (A.19)$$

$$\widehat{U_{12}^{e,\perp}}(k,l) = -\mathrm{i}\frac{\delta}{2}\frac{\sin\left(\frac{2\pi(k-1)}{N_1}\right)}{\cos\left(2\pi\left(\frac{(k-1)}{N_1}\right)\right)+\cos\left(2\pi\left(\frac{(l-1)}{N_2}\right)\right)-2}\widehat{G_{121}^{e,\perp}}(k,l) \quad (A.20)$$

$$\widehat{U_{21}^{e,\perp}}(k,l) = -\mathrm{i}\frac{\delta}{2}\frac{\sin\left(\frac{2\pi(l-1)}{N_2}\right)}{\cos\left(2\pi\left(\frac{(k-1)}{N_1}\right)\right)+\cos\left(2\pi\left(\frac{(l-1)}{N_2}\right)\right)-2}\widehat{G_{122}^{e,\perp}}(k,l) \quad (A.21)$$

and,

$$\widehat{U_{11}^{e,\perp}}(1,1) = \widehat{U_{11}^{e,\perp}}(1,1) = \widehat{U_{12}^{e,\perp}}(1,1) = \widehat{U_{21}^{e,\perp}}(1,1) = 0 \qquad (A.22)$$

Appendix B. FFT solution of Navier-type equations for single straight defects

Once $\widehat{U_{11}^{e,\perp}}, \widehat{U_{12}^{e,\perp}}, \widehat{U_{21}^{e,\perp}}, \widehat{U_{22}^{e,\perp}}$ are determined in the Fourier space (see Appendix A), the Navier-type equation (Eq. (41)) is solved using the intrinsic discrete Fourier transform method (Eqs. (57)–(68)) to derive $\widehat{w_1}$ and $\widehat{w_2}$ by assuming isotropic elasticity defined by the two elastic constants λ (Lamé constant) and μ (shear modulus). Thus, $\widehat{w_1}$ and $\widehat{w_2}$ are the solutions of the following linear algebraic system $\forall (k,l) \neq (1,1)$

$$\begin{pmatrix} A_{11}(k,l) & A_{12}(k,l) \\ A_{12}(k,l) & A_{22}(k,l) \end{pmatrix} \begin{pmatrix} \widehat{w_1}(k,l) \\ \widehat{w_2}(k,l) \end{pmatrix} = \begin{pmatrix} B_1(k,l) \\ B_2(k,l) \end{pmatrix} \qquad (B.1)$$

and,

$$\widehat{w_1}(1,1) = \widehat{w_2}(1,1) = 0 \qquad (B.2)$$

where

$$A_{11} = \frac{2}{\delta^2}\left[(\lambda+2\mu)\left(\cos\left(\frac{2\pi(k-1)}{N_1}\right)-1\right)+\mu\left(\cos\left(\frac{2\pi(l-1)}{N_2}\right)-1\right)\right] \quad (B.3)$$

$$A_{12} = \frac{(\lambda+\mu)}{2\delta^2}\times\left[\cos\left(2\pi\left(\frac{(k-1)}{N_1}+\frac{(l-1)}{N_2}\right)\right)-\cos\left(2\pi\left(\frac{(k-1)}{N_1}-\frac{(l-1)}{N_2}\right)\right)\right] \quad (B.4)$$

$$A_{22} = \frac{2}{\delta^2}\left[(\lambda+2\mu)\left(\cos\left(\frac{2\pi(l-1)}{N_2}\right)-1\right)+\mu\left(\cos\left(\frac{2\pi(k-1)}{N_1}\right)-1\right)\right] \quad (B.5)$$

$$B_1 = -\frac{\mathrm{i}}{\delta}\left[(\lambda+2\mu)\sin\left(\frac{2\pi(k-1)}{N_1}\right)\widehat{U_{11}^{e,\perp}}+\lambda\sin\left(\frac{2\pi(k-1)}{N_1}\right)\widehat{U_{22}^{e,\perp}}\right] \\ -\frac{\mathrm{i}}{\delta}\left[\mu\sin\left(\frac{2\pi(l-1)}{N_2}\right)\left(\widehat{U_{12}^{e,\perp}}+\widehat{U_{21}^{e,\perp}}\right)\right] \qquad (B.6)$$

$$B_2 = -\frac{\mathrm{i}}{\delta}\left[(\lambda+2\mu)\sin\left(\frac{2\pi(l-1)}{N_2}\right)\widehat{U_{22}^{e,\perp}}+\lambda\sin\left(\frac{2\pi(l-1)}{N_2}\right)\widehat{U_{11}^{e,\perp}}\right] \\ -\frac{\mathrm{i}}{\delta}\left[\mu\sin\left(\frac{2\pi(k-1)}{N_1}\right)\left(\widehat{U_{12}^{e,\perp}}+\widehat{U_{21}^{e,\perp}}\right)\right] \qquad (B.7)$$

Hence, the compatible elastic distortions $\widehat{U_{11}^{e,\|}}(k,l), \widehat{U_{22}^{e,\|}}(k,l),$ $\widehat{U_{12}^{e,\|}}(k,l), \widehat{U_{21}^{e,\|}}(k,l)$ are obtained as follows

$$\widehat{U_{11}^{e,\|}}(k,l) = \frac{\mathrm{i}}{\delta}\sin\left(\frac{2\pi(k-1)}{N_1}\right)\widehat{w_1}(k,l) \qquad (B.8)$$

$$\widehat{U_{22}^{e,\|}}(k,l) = \frac{\mathrm{i}}{\delta}\sin\left(\frac{2\pi(l-1)}{N_2}\right)\widehat{w_2}(k,l) \qquad (B.9)$$

$$\widehat{U_{12}^{e,\|}}(k,l) = \frac{\mathrm{i}}{\delta}\sin\left(\frac{2\pi(l-1)}{N_2}\right)\widehat{w_1}(k,l) \qquad (B.10)$$

$$\widehat{U_{21}^{e,\|}}(k,l) = \frac{\mathrm{i}}{\delta}\sin\left(\frac{2\pi(k-1)}{N_1}\right)\widehat{w_2}(k,l) \qquad (B.11)$$

Then, the stress components in the discrete Fourier space follow from $\widehat{U_{ij}^{e}}(k,l) = \widehat{U_{ij}^{e,\|}}(k,l) + \widehat{U_{ij}^{e,\perp}}(k,l)$ and from the application of the Hooke's law (Eq. (53)).

References

Acharya, A., 2001. A model of crystal plasticity based on the theory of continuously distributed dislocations. J. Mech. Phys. Solids 49, 761–785.

Acharya, A., Fressengeas, C., 2012. Coupled phase transformations and plasticity as a field theory of deformation incompatibility. Int. J. Fract. 174, 87–94.

Acharya, A., Roy, A., 2006. Size effects and idealized dislocation microstructure at small scales: predictions of a Phenomenological model of mesoscopic field dislocation mechanics: part I. J. Mech. Phys. Solids 54, 1687–1710.

Anglin, B.S., Lebensohn, R.A., Rollett, A.D., 2014. Validation of a numerical method based on Fast Fourier Transforms for heterogeneous thermoelastic materials by comparison with analytical solutions. Comput. Mater. Sci. 87, 209–217.

Bilby, B.A., Bullough, R., Smith, E., 1955. Continuous distributions of dislocations: a new application of the methods of non-riemannian geometry. Proc. R. Soc. London A 231, 263–273.

Brenner, R., Beaudoin, A.J., Suquet, P., Acharya, A., 2014. Numerical implementation of static field dislocation mechanics theory for periodic media. Philos. Mag. 94 (16), 1764–1787.

Brisard, S., Dormieux, L., 2010. FFT-based methods for the mechanics of composites: a general variational framework. Comput. Mater. Sci. 49, 663–671.

Christian, J.W., Mahajan, S., 1995. Deformation twinning. Prog. Mater. Sci. 39, 1–157.

deWit, R., 1960. The continuum theory of stationary dislocations. Solid State Phys. 10, 269–292.

deWit, R., 1970. Linear theory of static disclinations. In: Simmons, J.A., de Wit, R., Bullough, R. (Eds.), Fundamental Aspects of Dislocation Theory, NBS Spec. Publ. 317, vol. 1. National Bureau of Standards, Washington, DC, pp. 651–680.

deWit, R., 1973. Theory of disclinations: IV Straight disclinations. J. Res. Nat. Bur. Stand. A. Phys. Chem. 77A (5), 607–658.

Dreyer, W., Müller, W.H., Olschewski, J., 1999. An approximate analytical 2D-solution for the stresses and strains in eigenstrained cubic materials. Acta Mech. 136 (3–4), 171–192.

Eisenlohr, P., Diehl, M., Lebensohn, R.A., Roters, F., 2013. A spectral method solution to crystal elasto-viscoplasticity at finite strains. Int. J. Plast. 46, 37–53.

Eyre, D.J., Milton, G.W., 1999. A fast numerical scheme for computing the response of composites using grid refinement. Eur. Phys. J. Appl. Phys. 6, 41–47.

FFTW, 1998. <http://www.fftw.org>

Fressengeas, C., Acharya, A., 2014. Analytical stress/strain field of straight g-disclinations. Private communication.

Fressengeas, C., Taupin, V., Capolungo, L., 2011. An elasto-plastic theory of dislocation and disclination fields. Int. J. Solids Struct. 48, 3499–3509.

Fressengeas, C., Taupin, V., Capolungo, L., 2014. Continuous modeling of the structure of symmetric tilt boundaries. Int. J. Solids Struct. 51, 1434–1441.

Hecht, F., 2012. New development in FreeFEM++. J. Numer. Math. 20 (3–4), 251–265.

Herrmann, K., Müller, W., Neumann, S., 1999. Linear and elastic-plastic fracture mechanics revisited by use of Fourier Transforms: theory and application. Comput. Mater. Sci. 6, 186–196.

Hirth, J.P., Lothe, J., 1982. Theory of Dislocations, 2nd ed. Wiley, New York.

Hu, S.Y., Chen, L.Q., 2001. Solute segregation and coherent nucleation and growth near a dislocation: a phase-field model integrating defect and phase microstructure. Acta Mater. 49, 463–472.

Jiang, B., 1998. The least-squares finite element method. In: Theory and Computation in Fluid Dynamics and Electromagnetics. Springer Series in Scientific Computation. Springer, Berlin.

Kosevich, A.M., 1979. Crystal dislocations and the theory of elasticity (chap. 1). In: Nabarro, F.R.N. (Ed.), Dislocations in Solids, vol. 1. North-Holland, Amsterdam, pp. 33–141.

Kröner, E., 1958. Kontinuumstheorie der Versetzungen und Eigenspannungen. In: Collatz, L., Loesch, F. (Eds.), Ergebnisse der Angewewandte Mathematik, 5. Springer Verlag, Berlin.

Kröner, E., 1981. Continuum theory of defects. In: Balian, R. et al. (Eds.), Physics of Defects, Les Houches, Session 35. North Holland, New York, pp. 215–315.

Kröner, E., 1989. Modified Green functions in the theory of heterogeneous and/or anisotropic linearly elastic media. In: Weng, G.J., Taya, M., Abe, M. (Eds.). Springer Verlag, Berlin Germany.

Lebensohn, R., 2001. N-site modeling of a 3D viscoplastic polycrystal using Fast Fourier Transform. Acta Mater. 49, 2723–2737.

Lebensohn, R.A., Kanjarla, A.K., Eisenlohr, P., 2012. An elasto-viscoplastic formulation based on Fast Fourier Transforms for the prediction of micromechanical fields in polycrystalline materials. Int. J. Plast. 32–33, 59–69.

Matlab, 2012. Fast Fourier Transforms: FFT. MathWorks France.

Michel, J.C., Moulinec, H., Suquet, P., 2001. A computational scheme for linear and non-linear composites with arbitrary phase contrast. Int. J. Numer. Methods Eng. 52, 139–160.

Monchiet, V., Bonnet, G., 2013. Numerical homogenization of nonlinear composites with a polarization-based FFT iterative scheme. Comput. Mater. Sci. 79, 276–283.

Moulinec, H., Suquet, P., 1994. A fast numerical method for computing the linear and non linear properties of composites. C.R. Acad. Sci. Paris II 318, 1417–1423.

Moulinec, H., Suquet, P., 1998. A numerical method for computing the overall response of nonlinear composites with complex microstructure. Comput. Methods Appl. Mech. Eng. 157, 69–94.

Müller, W.H., 1996. Mathematical vs. experimental stress analysis of inhomogeneities in solids. J. Phys. IV 6 (C1), 139–148.

Müller, W.H., 1998. Fourier transforms and their application to the formation of textures and changes of morphology in solids. In: IUTAM Symposium on Transformation Problems in Composite and Active Materials. Kluwer Academic Publishers, pp. 61–72.

Mura, T., 1963. Continuous distribution of moving dislocations. Philos. Mag. 89, 843–857.

Mura, T., 1987. Micromechanics of Defects in Solids. Kluwer Academic Publishers, Dordrecht, The Netherlands.

Neumann, S., Herrmann, K., Müller, W., 2002. Stress/strain computation in heterogeneous bodies with Discrete Fourier Transforms – different approaches. Comput. Mater. Sci. 25, 151–158.

Prakash, A., Lebensohn, R.A., 2012. Simulation of micro mechanical behavior of polycrystals: Finite Elements versus Fast Fourier Transforms. Modell. Simul. Mater. Sci. Eng. 17, 64010–64016.

Press, W.H., Teukolsky, S.A., Vetterling, W.T., Flannery, B.P., 2002. Numerical Recipes in C++. The Art of Scientific Computing, 2nd ed. Cambridge University Press, USA.

Romanov, A.E., Vladimirov, V., 1992. Disclinations in crystalline solids (chap. 47). Dislocations in Solids, vol. 9. Elsevier Science Publishers B.V., pp. 191–402.

Roy, A., Acharya, A., 2005. Finite element approximation of field dislocation mechanics. J. Mech. Phys. Solids 53, 143–170.

Spahn, J., Andrä, H., Kabel, M., Müller, R., 2014. A multiscale approach for modeling progressive damage of composite materials using Fast Fourier Transforms. Comput. Methods Appl. Mech. Eng. 268, 871–883.

Upadhyay, M., Capolungo, L., Taupin, V., Fressengeas, C., 2013. Elastic constitutive laws for incompatible crystalline media: the contributions of dislocations, disclinations and g-disclinations. Philos. Mag. 93, 794–832.

Vinogradov, V., Milton, G.W., 2008. An accelerated FFT algorithm for thermoelastic and non-linear composites. Int. J. Numer. Methods Eng. 76, 1678–1695.

Volterra, S., 1907. Sur l'équilibre des corps élastiques multiplement connexes. Ann. Sci. Ecol. Norm. Sup. III 24, 401–517.

Willis, J.R., 1967. Second-order effects of dislocations in anisotropic crystals. Int. J. Eng. Sci. 5, 171–190.

Willis, J.R., 1981. Variational and related methods for the overall properties of composites. Adv. Appl. Mech. 21, 1–78.

Willot, F., Abdallah, B., Pellegrini, Y.P., 2014. Fourier-based schemes with modified Green operator for computing the electrical response of heterogeneous media with accurate local fields. Int. J. Numer. Methods Eng. 98, 518–533.